

AdS/CFT with Flavour in Electric and Magnetic Kalb-Ramond Fields

Johanna Erdmenger & René Meyer

*Max Planck-Institut für Physik (Werner Heisenberg-Institut)
Föhringer Ring 6, 80805 München, Germany
E-mail: jke@mppmu.mpg.de, meyer@mppmu.mpg.de*

Jonathan P. Shock

*Institute of Theoretical Physics, Chinese Academy of Sciences
P.O. Box 2735, Beijing 100080, People's Republic of China
Email: shock@fpaxp1.usc.es*

ABSTRACT: We investigate gauge/gravity duals with flavour for which pure-gauge Kalb-Ramond B fields are turned on in the background, into which a D7 brane probe is embedded. First we consider the case of a magnetic field in two of the spatial boundary directions. We show that at finite temperature, i.e. in the AdS-Schwarzschild background, the B field has a stabilizing effect on the mesons and chiral symmetry breaking occurs for a sufficiently large value of the B field. Then we turn to the electric case of a B field in the temporal direction and one spatial boundary direction. In this case, there is a singular region in which it is necessary to turn on a gauge field on the brane in order to ensure reality of the brane action. We find that the brane embeddings are attracted towards this region. Far away from this region, in the weak field case at zero temperature, we investigate the meson spectrum and find a mass shift similar to the Stark effect.

KEYWORDS: [AdS-CFT correspondence](#), [Brane Dynamics in Gauge Theories](#).

Contents

1. Introduction and Summary	1
2. Fundamental matter in external fields at zero temperature	4
2.1 General ansatz	4
2.2 Magnetic Kalb-Ramond field at zero temperature	5
3. Magnetic Kalb-Ramond field at finite temperature	7
4. Electric Kalb-Ramond field	12
4.1 Electric field at zero temperature	12
4.1.1 Embeddings	14
4.1.2 Meson spectrum	17
4.2 Stark effect	18
4.3 Electric Kalb-Ramond field at finite temperature	22
5. Conclusions and Outlook	24
A. Some useful expansion formulae	27
B. Decoupling of Φ-fluctuations	27

1. Introduction and Summary

In the last decade we have seen major advances in the understanding of strongly coupled gauge theories through the AdS/CFT correspondence and its generalisations. The breaking of supersymmetry in deformed supergravity backgrounds and the addition of fundamental matter using brane probes has allowed a study of QCD-like theories and many measurable quantities thereof. An example of this is the embedding of probe D7 branes [1]. The comparison to real-world QCD is often at the level of a few percent. In particular, gravity dual constructions describing spontaneous chiral symmetry breaking have been found in [2–5], and are relevant for the light-quark sector of QCD. The exploration of the phase structure of this sector is ongoing [2, 6–18].

In this paper we consider the effect of an external Kalb-Ramond B field for D7 branes embedded in a (dual) gravity background. Our motivation to look at such configurations originates from the investigations in [19, 20], where D7 brane probes were embedded into the Polchinski-Strassler background [21]. In this background, a B field of quite complicated structure, dependent on the radial coordinate of the dual space, is turned on in all six directions perpendicular to the boundary. In the original work of Polchinski and Strassler

[21] this has been shown to correspond to mass terms for the adjoint chiral multiplets in the dual gauge theory. For the theory with added flavour, this implies a repulsion of the D7 branes by the shell forming in the background due to the Myers effect [22]. This leads to a shift of the meson spectrum induced by the adjoint masses (for details to second order in the adjoint masses see [19]).

In contrast, in [23] a pure-gauge magnetic Kalb-Ramond field was turned on in two spatial directions of the D3-brane world-volume, parallel to the boundary. This was found to induce chiral symmetry breaking and a Zeeman splitting of the meson states. This setup was investigated further in [24]. A related approach using both external magnetic and electric fields was used in [25–27] to calculate conductivities and to study the holographic Hall effect (for related work in 2+1 dimensions see also [28]).

In the present paper, we consider both external magnetic and electric fields separately. In the electric case, the B field extends into the temporal direction and one spatial direction parallel to the boundary. We begin by considering the magnetic B field of [23] in the AdS-Schwarzschild background dual to a finite-temperature field theory, and study the phase structure of one fundamental hypermultiplet in this background by embedding a probe D7 brane in it. We see two competing mechanisms at work: As first discussed in [2], the black hole attracts the D7 brane which bends towards it. For very large values of the quark mass in units of the temperature, as determined by the UV boundary value of the D7 embedding, this leads to a very small value of the quark condensate. Moreover, for brane probes ending on the black hole, there is a phase in which mesons are unstable and melt in the $\mathcal{N} = 4$ plasma. The melting transition for the mesons occurs when the D7 brane probe reaches the black hole horizon. On the other hand, as discussed in [23], the magnetic B field leads to spontaneous chiral symmetry breaking, since the quark condensate is large even at zero quark mass. This is essentially due to the fact that the magnetic B field has the effect of repelling the D7 probe from the origin. Here we find that for sufficiently large B field, the second mechanism is stronger than the first one and we find spontaneous chiral symmetry breaking even in the black hole background. A critical line in the $T - B$ phase diagram illustrates the interplay between the two effects: The magnetic field acts by repelling the embeddings from the horizon. Above a critical value for the field strength (at a fixed temperature) this repulsion is so strong that no embedding, not even the embedding corresponding to massless quarks, can flow into the black hole any more - all embeddings are Minkowski embeddings for which the meson spectrum is discrete. For fixed mass, varying the temperature, this is equivalent to stating that for increasing magnetic field the critical temperature for the melting phase transition increases. We also investigate the meson spectrum for this scenario and find that a Goldstone mode occurs above the critical B field value, in agreement with spontaneous chiral symmetry breaking.

Moreover, we also consider the case where the B field is turned on in spatio-temporal directions, corresponding to an external electric field in the gauge theory. In this case there is a singular region with topology S^5 where the Dirac-Born-Infeld action for the D7 brane has a zero and becomes tachyonic. It is necessary to turn on a gauge field on the brane in order to ensure a regular action beyond the shell where the brane action vanishes, similar to [25]. The singular shell of vanishing brane action has an attracting effect on the D7

brane probes, as opposed to the repulsion observed in the magnetic case. This may be interpreted as the holographic incarnation of an ionization effect.

Far away from this region, i.e. in the weak field limit at zero temperature, we investigate the meson spectrum both analytically and numerically and find a mass shift for the pseudoscalar mesons $\delta M \sim B^2$. This is very similar to the second-order Stark effect for atoms in electric fields, where the energy levels of s -orbitals are shifted by an amount proportional to the square of the applied field strength. For the analytical calculation, we perform a perturbative analysis in the external field to lowest order.

We also consider the case of a general, not necessarily small, electric field strength. After obtaining a regular action as in [25] by introducing gauge fields on the brane, we find that both at zero and finite temperature regular embeddings exist which pass through the shell of vanishing action. Our ansatz for the world volume gauge field corresponds to baryon number densities and currents in the dual gauge theory, and we are considering the canonical ensemble, in which the baryon number density is fixed. Minkowski embeddings can only exist if the baryon density vanishes [12], and this is the situation we will be mostly interested in. Besides Minkowski embeddings, we find two different classes at zero temperature: Embeddings that reach all the way to the (extremal) horizon of AdS space, and, at quark masses between the Minkowski embeddings and the ones ending at the AdS horizon, embeddings which end in a conical singularity, the latter of which were first noticed in [30]. At finite temperature and for vanishing baryon densities, we find, in order of decreasing asymptotic quark mass, Minkowski embeddings, conically singular embeddings and those that fall into the black hole. Both at zero and finite temperature, we expect a first order phase transition between the Minkowski and singular shell embeddings, which we associate with mesons dissociation due to the external electric field. The physical meaning of the conically singular embeddings, in particular their stability and role in this phase transition, remains to be investigated. At finite baryon number density and temperature, we find that black hole embeddings exist, covering the whole range of asymptotic quark mass. As Minkowski embeddings are inconsistent in that case, the dissociation phase transition should then occur between different black hole embeddings, similar to the situation in the canonical ensemble without electric field [12].

This paper is organized as follows: We begin by considering the general ansatz for both magnetic and electric fields in section 2, and comment on some aspects of the magnetic case at zero temperature in particular. In section 3 we consider the magnetic case at finite temperature and show that spontaneous chiral symmetry breaking occurs even at finite temperature above a critical value of the magnetic field strength. In section 4 we consider the electric case. In particular, we derive the meson mass shift which corresponds to the Stark effect. Moreover we discuss the behaviour of the embeddings for general, not necessarily small, values of the Kalb-Ramond field. We conclude briefly in section 5 with a discussion of the instability which potentially occurs for the electric B-field, and differences between the canonical and grand canonical ensemble in the electric case. Some calculational details are relegated to two appendices.

While preparing this paper, we became aware of the fact that two papers on the same subject are being prepared by T. Albash, V. Filev, C. Johnson and A. Kundu [29,30].

2. Fundamental matter in external fields at zero temperature

In [23] a pure gauge magnetic Kalb-Ramond field was added to the $AdS_5 \times S^5$ geometry and quenched fundamental matter was included using a D7 brane probe. The D7 brane embeddings were calculated and it was found that chiral symmetry is spontaneously broken, as indicated by a non-zero quark condensate at vanishing quark mass. The spectrum of mesons was also calculated both for small and large magnetic field strength and the Goldstone mode was found to satisfy the Gell-Mann-Oakes-Renner relation [31].

In this section we review the results of [23]. Moreover we simultaneously consider a new ansatz for the Kalb-Ramond field, corresponding to an electric field.

2.1 General ansatz

We deal in parallel with the magnetic and electric ansätze for the Kalb-Ramond field.

The background of interest is the pure AdS geometry, given by

$$ds^2 = \frac{\omega^2}{R^2} (dx_0^2 + d\vec{x}^2) + \frac{R^2}{\omega^2} (d\rho^2 + \rho^2 d\Omega_3^2 + dL^2 + L^2 d\Phi^2). \quad (2.1)$$

Here the AdS radial coordinate is given by $\omega^2 = \rho^2 + L^2$. For the S^3 we use Hopf coordinates

$$d\Omega_3^2 = d\psi^2 + \cos^2 \psi d\beta^2 + \sin^2 \psi d\gamma^2. \quad (2.2)$$

In addition, the background involves the usual four-form and constant dilaton

$$g_s C_{(4)} = \frac{\omega^4}{R^4} dx^0 \wedge dx^1 \wedge dx^2 \wedge dx^3, \quad e^{\phi_\infty} = g_s, \quad R^4 = 4\pi g_s N \alpha'^2. \quad (2.3)$$

There are two obvious choices of a pure gauge ansatz for the Kalb-Ramond fields¹,

$$B_{(2)m} = B dx_2 \wedge dx_3, \quad B_{(2)e} = B dx_0 \wedge dx_1. \quad (2.4)$$

We label these the magnetic and electric ansatz, respectively, as, after embedding a D7 brane in the background and trading the constant B field for the $U(1)_F$ gauge field on the brane via $F_{\mu\nu} = -\frac{B_{\mu\nu}}{2\pi\alpha'}$, the two choices correspond to constant electric and magnetic field strengths. Both these pure-gauge ansätze are solutions to the IIB supergravity equation of motion (see eg. [21]). Provided that $C_2 = 0$, which ensures the absence of a boundary term $d(C_2 \wedge B)$, the B field does not deform the $AdS_5 \times S^5$.

In this work, we will always choose static gauge $\xi^a = (x^\mu, \rho, \psi, \beta, \gamma)$, for the D7 brane, and parametrize its embedding by an ansatz $L = L(\rho)$, $\Phi = 0$, thus preserving the rotational symmetry of the S^3 wrapped by the D7 brane. The rotational symmetry perpendicular to the D7 brane will be broken for nonzero embeddings L . In the background (2.1) and for the two B fields (2.4), the DBI action is given by

$$\mathcal{L}_{m,e} = -\frac{T_7}{g_s} \rho^3 \sin \psi \cos \psi \sqrt{1 + L'^2} \sqrt{1 \pm \frac{R^4 B^2}{(\rho^2 + L^2)^2}}, \quad (2.5)$$

¹A third choice, as pointed out to us by P. Aschieri, would be a light-like B field. It has the advantage that for spacelike (i.e. magnetic) or lightlike B , there is a decoupling limit leading to a noncommutative field theory [32,33], while in the electric or timelike case the best one can do is to decouple the closed string modes [34–36]. This then corresponds to non-commutative open string theory.

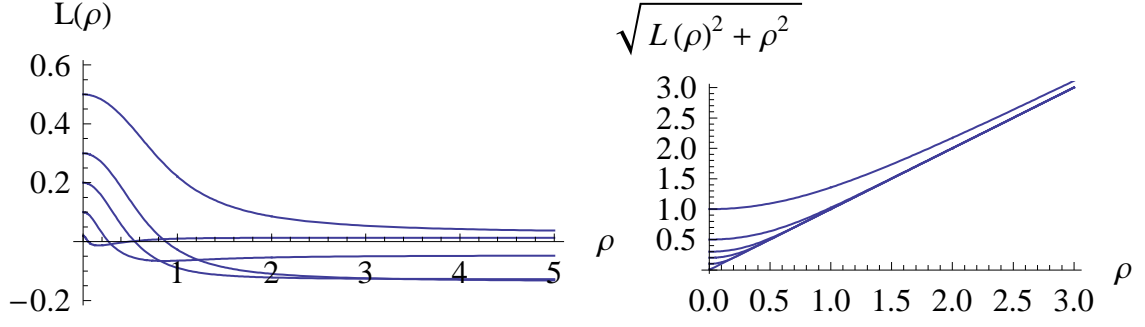


Figure 1: D7 brane embeddings in $AdS_5 \times S^5$ with external magnetic field.

where the positive (negative) sign corresponds to the magnetic (electric) ansatz, and ψ is one of the Hopf coordinate angles defined in (2.2). The Wess-Zumino part of the D7 action does not contribute, as $P[C_4] \wedge B_{(2)m,e} = 0$ and the pullback of the magnetic dual of C_4 vanishes, $P[\tilde{C}_4] = 0$. The D7 brane embedding is found by solving the Euler-Lagrange equation for $L(\rho)$,

$$0 = \partial_\rho \left(\frac{\rho^3 L' \sqrt{1 \pm \frac{B^2 R^4}{(\rho^2 + L^2)^2}}}{\sqrt{1 + L'^2}} \right) \pm \frac{2B^2 R^4 \rho^3 L \sqrt{1 + L'^2}}{(\rho^2 + L^2)^3 \sqrt{1 \pm \frac{B^2 R^4}{(\rho^2 + L^2)^2}}}, \quad (2.6)$$

which is a scalar from the point of view of the world volume field theory. In both the magnetic and electric cases, the UV (i.e. large ρ) behaviour of the embeddings is given by

$$L(\rho) \sim m + \frac{c}{\rho^2}, \quad (2.7)$$

i.e. the embeddings asymptote to the pure $AdS_5 \times S^5$ solution $L = m$ for $\rho \rightarrow \infty$. The quantity m is proportional to the quark mass, $m_q = m/2\pi\alpha'$, while c is related to the chiral condensate via² $\langle \bar{q}q \rangle = c/(2\pi\alpha')^3$. As discussed in [23], supersymmetry is broken on the brane, though not in the background.

2.2 Magnetic Kalb-Ramond field at zero temperature

We now review the results of [23] for the magnetic case at zero temperature. Some examples for the embedding in the magnetic case with varying IR boundary are shown in figure 1. For completeness we have also shown solutions with negative quark mass as fixed by the UV asymptotic behaviour. For small quark mass, the embeddings intersect the ρ axis, in some cases several times. We will show that these solutions describe a well-behaved renormalization group flow, in contrast to the argument in [23]. Nevertheless these solutions are ruled out by an energy argument which shows that they are not the lowest-energy configurations. Although the D7 brane does cross the ρ axis multiple times

²Because of supersymmetry, c would also contain squark terms. We assume in this work that the squarks have zero vacuum expectation value [12].

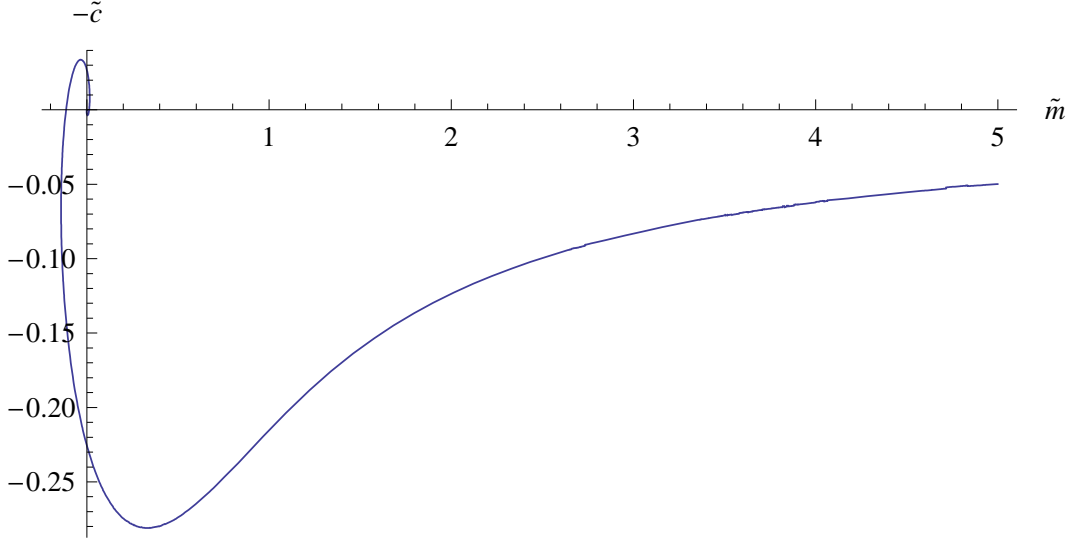


Figure 2: $-\tilde{c}(\tilde{m})$ for the magnetic ansatz at $T = 0$.

for small quark masses, it does not indicate a multiple intersection with the D3-brane stack. The distance of the D7 brane from the origin of the (ρ, L) plane is monotonically decreasing as the solution flows towards the IR. This can be seen in the right hand graph of figure 1.

In the normalization of [23], for which we perform a rescaling $\rho \rightarrow R\sqrt{B}\rho$, $L \rightarrow R\sqrt{B}L$, the equation of motion is given by

$$0 = \partial_\rho \left(\frac{\rho^3 L' \sqrt{1 + \frac{1}{(\rho^2 + L^2)^2}}}{\sqrt{1 + L'^2}} \right) + \frac{2\rho^3 L \sqrt{1 + L'^2}}{(\rho^2 + L^2)^3 \sqrt{1 + \frac{1}{(\rho^2 + L^2)^2}}} . \quad (2.8)$$

The UV asymptotics of the solutions is

$$L(\rho) = \tilde{m} + \frac{\tilde{c}}{\rho^2}, \quad \tilde{m} = \frac{2\pi\alpha' m_q}{R\sqrt{B}}, \quad \tilde{c} = \langle \bar{q}q \rangle \frac{(2\pi\alpha')^3}{R^3 B^{\frac{3}{2}}} . \quad (2.9)$$

The extra factor of B in the normalization is convenient in the zero temperature case. Using (2.9), we can extract the rescaled mass and condensate from the numerically determined D7 embeddings. It was found in [23] that $\tilde{c}(\tilde{m})$ shows a self-similar spiral behaviour. This indicates that for a given quark mass, there may be more than one solution. It is thus important to understand which of the solutions is physical.

It was stated in [23] that the inner arms of the spiral intersect with the D3 branes multiple times, and thus only the outer portion of the spiral in the lower right quadrant of figure 2 is physical. We now show that this conclusion may be found through simple energy considerations. In order to determine which of the degenerate solutions is the physical one, we calculate the energy of each solution. The energy of each one has a UV divergence which must be removed by an appropriate normalisation. For the purposes of our calculation, it is sufficient simply to impose a cutoff Λ , which is sent to infinity at the end, and subtract

a reference solution ³,

$$E_{norm} = \int_{\rho_0}^{\Lambda} d\rho \rho^3 \sqrt{1 + L_0'(\rho)^2} \sqrt{1 \pm \frac{B^2 R^4}{(\rho^2 + L_0(\rho)^2)^2}} - E_{ref} , \quad (2.10)$$

where

$$E_{ref} = \int_{\rho_0}^{\Lambda} d\rho \rho^3 \sqrt{1 + L_{ref}'(\rho)^2} \sqrt{1 \pm \frac{B^2 R^4}{(\rho^2 + L_{ref}(\rho)^2)^2}} . \quad (2.11)$$

Here L_0 is the classical solution to the embedding equation of motion. The lower integration limit ρ_0 is zero for the magnetic case at zero temperature, as in that case the D7 brane fills the whole range $0 \leq \rho < \infty$. We use the physical $m = 0$ solution as a reference solution. This is just a convenient choice, as a shift of the normalized energy does not change the relative energies between physical and unphysical embeddings.

The $-\tilde{c}(\tilde{m})$ spiral in figure 2 cuts the $\tilde{m} = 0$ axis an infinite number of times, dividing the spiral in different branches in each quadrant of the (\tilde{m}, \tilde{c}) -plane. The physical embeddings are those which have the lowest energy according to (2.10). Figure 3 shows the $-\tilde{c}(\tilde{m})$ -spiral (green line) along with the corresponding normalized energy $E_{norm}(\tilde{m})$ (blue line). The dashed lines link $\tilde{m} = 0$ points on the condensate curve which correspond to massless embeddings, with the corresponding points on the normalized energy curve. The numbers next to the dashed lines are the values of the normalized energies for these massless embeddings. We find that the lowest energy configuration for zero quark mass is the one where the lowest branch of the condensate curve in the bottom right quadrant of figure 3 intersects the $-\tilde{c}$ -axis. It is also clear from figure 3 that the energy for the embeddings on this branch is indeed smaller than for all the other branches. The lowest lying branch in the bottom right quadrant of figure 3 thus corresponds to the physical embeddings, while the other branches have to be considered unphysical. As this physical branch admits a non-zero quark condensate $-\tilde{c}(0)$ at zero quark mass, spontaneous breaking of the $U(1)$ chiral symmetry is possible in the presence of the magnetic Kalb-Ramond field.

3. Magnetic Kalb-Ramond field at finite temperature

The embedding of D7 brane probes into the AdS-Schwarzschild black hole background, dual to a finite-temperature field theory, has first been studied in [2]. In the black hole background there is no spontaneous chiral symmetry breaking by a quark condensate, since the quark condensate vanishes for zero quark mass. On the other hand, there is an interesting first order phase transition [6] when the embedded D7 brane reaches the horizon. This has been studied in further detail by many authors [7–10], including the effect of a baryon chemical potential and of a finite baryon number density [14–17]. The embeddings

³As the energy for our static D7 brane configuration is just the negative of the action, we drop here all volume factors arising from integration over $(x^\mu, \psi, \beta, \gamma)$. Note that here we are not considering a holographic renormalisation and regularisation which is necessary for the correct calculation of the free energy and thermodynamic quantities [29]. In the coordinate system used in this work, no counterterms including m or c are necessary to cancel the large volume divergence $\propto \Lambda^4$, which is achieved by our subtraction method as well.

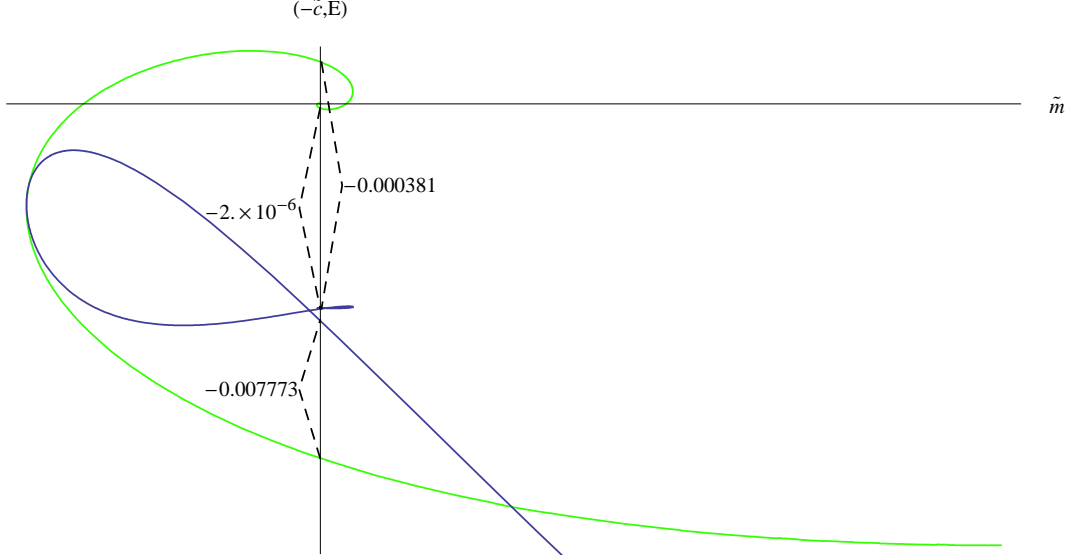


Figure 3: $-\tilde{c}(\tilde{m})$ for the magnetic ansatz (green line) and $E_{norm}(\tilde{m})$ (blue line). The numbers correspond to energies, and the dashed lines link corresponding points on the two curves. The origin of two plots are separated vertically by around 0.13 units. Note that the origin of the \tilde{c} axis does not coincide with the origin of the E_{norm} axis. See text for detailed explanation.

which terminate before reaching the horizon do so because the S^3 which they wrap shrinks to zero size, as discussed in [1]. The phase transition corresponds to the transition from the mesonic to the melted phase [11]. In the former there is a discrete meson spectrum with a mass gap, whereas in the latter the spectrum becomes continuous. The mesons melt at this phase transition due to the interaction with the hot $\mathcal{N} = 4$ plasma. Subsequently we will refer to D7 embeddings reaching the black hole horizon as black hole embeddings or as “in a melted phase”, while those which do not are named mesonic or Minkowski ones.

We now consider the effects of the Kalb-Ramond field (2.4) in the AdS-Schwarzschild background that is dual to a finite temperature field theory. The metric in Minkowski signature is given by ($\omega^2 = \rho^2 + L^2$)

$$ds^2 = \frac{\omega^2}{2R^2} \left(\frac{d\tilde{x}^2 (b^4 + \omega^4)}{\omega^4} - \frac{dt^2 (\omega^4 - b^4)^2}{\omega^4 (b^4 + \omega^4)} \right) + \frac{R^2}{\omega^2} (dL^2 + d\rho^2 + d\Phi^2 L^2 + \rho^2 d\Omega_3^2) . \quad (3.1)$$

The dilaton is constant for the black (i.e. non-extremal) D3 brane solution, whose near-horizon geometry is just (3.1) [37]. The temperature of the dual field theory is given by the Hawking temperature of the black hole

$$T = \frac{b}{\pi R^2} . \quad (3.2)$$

With the same static gauge as before, the DBI Lagrangian for a D7 brane probe in

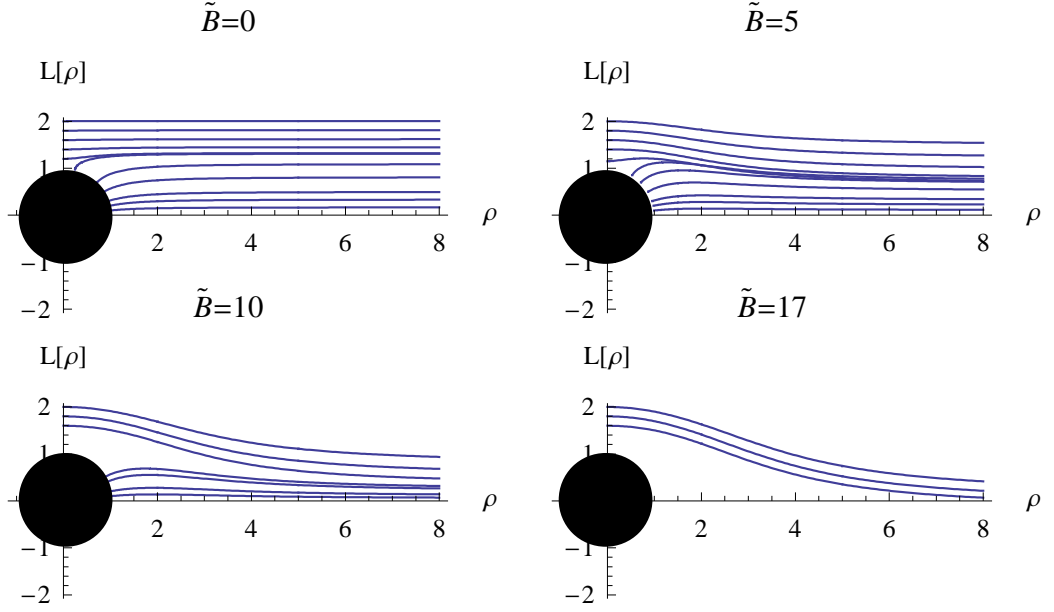


Figure 4: Increasing values of \tilde{B} for fixed T show the repulsive nature of the magnetic Kalb-Ramond field. We see that for large enough \tilde{B} , the melted phase is never reached, and the chiral symmetry is spontaneously broken.

this background reads for the magnetic (upper sign) and electric (lower sign) ansatz

$$\mathcal{L} = -\frac{T_7}{g_s} \cos \psi \sin \psi \frac{\tilde{\rho}^3 \left((\tilde{L}^2 + \tilde{\rho}^2)^2 \pm 1 \right)}{4(\tilde{L}^2 + \tilde{\rho}^2)^4} \times \\ \times \sqrt{\left(\left(1 \mp (\tilde{L}^2 + \tilde{\rho}^2)^2 \right) \mp \tilde{B}^2 (\tilde{L}^2 + \tilde{\rho}^2)^2 \right) (\tilde{L}^2 + 1)}. \quad (3.3)$$

Again, we have performed rescalings to dimensionless quantities $(L, \rho, B) = (b\tilde{L}, b\tilde{\rho}, \frac{\tilde{B}b^2}{2R^2})$, such that the horizon is at $\tilde{\rho}^2 + \tilde{L}^2 = 1$.

Let us now turn to the magnetic case. We numerically solve the Euler-Lagrange equation for $\tilde{L}(\tilde{\rho})$ obtained from the Lagrangian (3.3). It is convenient to introduce a rescaled B field

$$\hat{B} = \frac{B\lambda}{2\pi^2 R^2 m_q^2}, \quad (3.4)$$

as well as an appropriate dimensionless quark mass and condensate

$$m_q = \frac{1}{2} \sqrt{\lambda} T \tilde{m}, \quad \tilde{T} = \frac{1}{\tilde{m}}, \quad \langle \bar{q}q \rangle = -\frac{1}{8} \sqrt{\lambda} N_c T^3 \tilde{c}. \quad (3.5)$$

Here $\lambda = g_s N_c$ is the 't Hooft coupling.

The numerical results are plotted in figure 4 for increasing values of the magnetic field at a fixed temperature (or equivalently fixed Schwarzschild radius). We see that the increasing external magnetic field repels the branes from the horizon more and more,

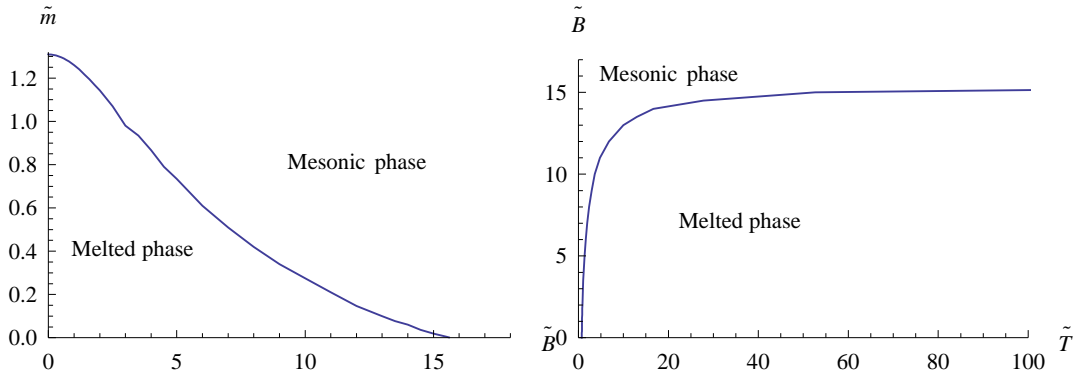


Figure 5: Phase diagram in the (\tilde{m}, \tilde{B}) and (\tilde{T}, \tilde{B}) planes for the magnetic Kalb-Ramond field. The graph on the left shows the largest quark mass for a given \tilde{B} for which the embedding still reaches the black hole. In the graph on the right, the critical line reaching a constant \tilde{B} at large temperature corresponds to a quadratic dependence $\hat{B}_{crit} \sim T^2$ at large temperature.

until there are no black hole solutions any more. This is exactly the point where the melted phase disappears, at a critical value $\tilde{B}_{crit} \approx 16$. In fact, above this critical value, there is spontaneous chiral symmetry breaking, since the lowest-energy solution at quark mass $\tilde{m} = 0$ is a mesonic one and has a condensate $\tilde{c} > 0$. On the other hand, in the case where the zero quark mass solution reaches the horizon and therefore corresponds to melted mesons, this solution is given by $L(\rho) = 0$ and thus no condensate develops and no spontaneous chiral symmetry breaking occurs.

The phase diagram is depicted in figure 5. On the left hand side we plot the largest quark mass \tilde{m} for given \tilde{B} for which the embedding still reaches the horizon. The temperature is fixed. We see that above the critical value $\tilde{B}_{crit} \approx 16$, there are no more black hole embeddings reaching the black hole horizon. On the right hand side of figure 5, we consider the same phase diagram for fixed \tilde{m} while varying \tilde{T} . We see that for large \tilde{T} , the critical value \tilde{B}_{crit} tends to a constant value around 16. Because \tilde{B} is explicitly a function of T , the appropriate dimensionless quantities to plot on the (T, B) phase diagram are (\tilde{T}, \hat{B}) . Because \tilde{B}_{crit} becomes constant for large \tilde{T} , we see that \hat{B}_{crit} behaves as \tilde{T}^2 for large \tilde{T} , corresponding to large temperature at fixed quark mass.

The condensate as a function of the mass for different \tilde{B} is shown in figure 17, which can be found at the end of this work: The blue part of the curve corresponds to the mesonic phase, while the green part at small quark masses corresponds to the melted phase. Increasing the magnetic field strength lowers the critical quark mass at which the first order phase transition occurs, until zero quark mass is reached at the critical value \tilde{B}_{crit} . At this point there is no melted phase any more, but a non-zero condensate at zero quark mass indicates spontaneous chiral symmetry breaking in the dual gauge theory. It should be noted that for a given quark mass there may be several possible embeddings. Just as in the case of pure finite temperature or pure magnetic field, the physical solutions can be found by energy considerations.

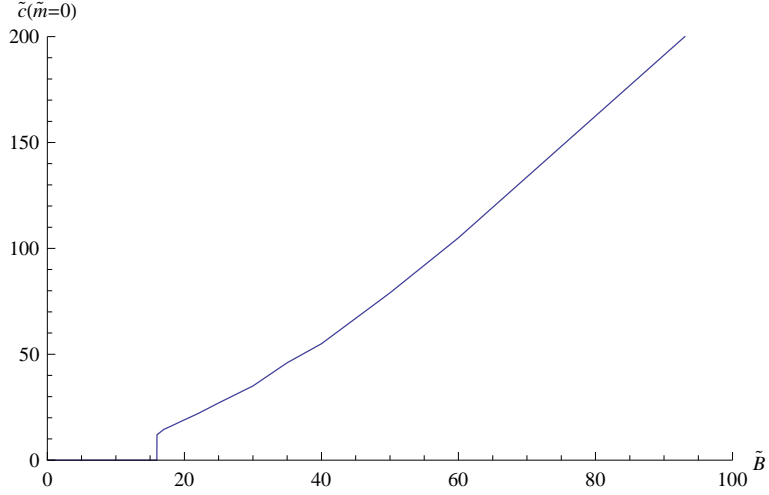


Figure 6: Condensate for the lowest-energy embedding at zero quark mass $\tilde{c}(0)$ as function of the magnetic field \tilde{B} . There is a first-order phase transition at which spontaneous chiral symmetry breaking occurs.

Yet another graph showing clearly the onset of spontaneous chiral symmetry breaking at the critical value of the magnetic B field is figure 6, in which the condensate at zero quark mass is plotted versus the external magnetic field. We observe that the phase transition is first order, as there is a jump in the order parameter \tilde{c} .

We also calculate meson masses for the Minkowski embeddings in the magnetic finite temperature background by solving the eigenvalue problem for the Φ -fluctuations. These correspond to pseudoscalar mesons, and we restrict ourselves to states with zero S^5 angular momentum $l = 0$. This calculation was performed at zero temperature in [23], where it was found (see also appendix B) that it is possible to decouple the gauge field fluctuations on the brane from the fluctuations of the embedding coordinate Φ , if the latter depends only on the coordinates (x^2, x^3) . These modes can be thought of as representing a meson in the euclidean (x^2, x^3) -plane [23]. We follow the same strategy and thus use the ansatz

$$\phi(\rho, x^2, x^3) = h(\rho)e^{-ik_2x_2 - ik_3x_3}. \quad (3.6)$$

The Lagrangian for the fluctuations reads

$$\begin{aligned} \mathcal{L} = & -\frac{1}{2} \frac{T_7}{g_s} \cos \psi \sin \psi \rho^3 \sqrt{g_{\rho\rho}^4 g_{x^1x^1}^3 g_{tt}} \left(\frac{B^2}{g_{x^1x^1}^2} + 1 \right) (L'^2 + 1) \times \\ & \times g_{\phi\phi} \left(\frac{g_{x^1x^1} ((\partial_2 \phi(\rho, x^2, x^3))^2 + (\partial_3 \phi(\rho, x^2, x^3))^2)}{(B^2 + g_{x^1x^1}^2)} + \frac{(\partial_\rho \phi(\rho, x^2, x^3))^2}{g_{\rho\rho} (L'^2 + 1)} \right), \end{aligned} \quad (3.7)$$

where the metric is given by (3.1).

The meson masses are obtained from

$$M^2 = -k_2^2 - k_3^2. \quad (3.8)$$

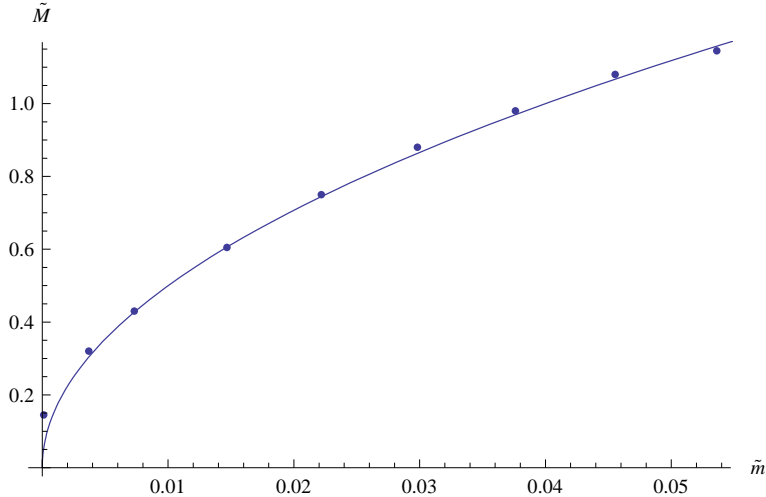


Figure 7: Mass of the Goldstone boson for $\tilde{B} = 16$. The solid line is the fitted curve $\tilde{M} = 5\sqrt{\tilde{m}}$, showing the typical Gell-Mann-Oakes-Renner behaviour.

The meson spectrum for fixed temperature and different B field values is plotted in figure 18, where the dashed lines are the pure AdS result $\tilde{M} = 2\tilde{m}\sqrt{(n+1)(n+2)}$, cf. [44]. The mesons in the magnetic case are heavier than their pure AdS counterparts, from which we conclude that the magnetic B field lowers the binding energy $E_b < 0$ and thus has a confining effect on the mesons. We find that above the critical magnetic field strength $\tilde{B}_{crit} \approx 16$, the lowest-lying meson state becomes massless for zero quark mass and thus is the Goldstone mode of chiral symmetry breaking. Figure 7 zooms into the zero mass region for this state, calculated for $\tilde{B} = 16$. The solid curve, $\tilde{M} = 5\sqrt{\tilde{m}}$, is obtained by fitting to the data points, and shows that our identification of this state with the Goldstone mode of chiral symmetry breaking is correct, as it satisfies the Gell-Mann-Oakes-Renner relation [31]. The deviation of the data point for the lowest reduced quark mass \tilde{m} is due to numerical artefacts.

4. Electric Kalb-Ramond field

4.1 Electric field at zero temperature

We now turn to the case when the Kalb-Ramond B field is switched on in the spatio-temporal directions, corresponding to an external electric field. There is a subtle but important difference between the Lagrangians for the magnetic and electric ansatz (2.5): In the case of the electric field, there is a zero of the action at $\omega^2 \equiv \rho^2 + L^2 = BR^2$. We name the five-sphere defined by this equation the *singular shell*. Generically, we find that in contrast to the magnetic case where the external field has a repulsive effect, now the singular shell is attracting the D7 solutions, in a sense similar to the black hole metric.

For values of the radius ω inside the singular shell, the DBI Lagrangian (2.5) becomes imaginary, which indicates a tachyonic instability [38–41]. We stabilize the D7 configuration by switching on a compensating gauge field on the D7 brane near and inside the singular

shell, along the lines of [25, 26]: We switch on components of the gauge field's Faraday tensor which correspond holographically to a finite baryon number density and a baryon number current expectation value $\langle J_x \rangle$. Demanding the DBI action to be real throughout ten-dimensional spacetime then imposes a regularity constraint relating number density and current.⁴

Using the ansatz of [25],

$$A_x = -f(\rho), \quad A_t = -g(\rho), \quad (4.1)$$

the action for the D7 brane in the external electric B field takes the form⁵

$$S_{D7} = -\mathcal{N} \int d\rho \rho^3 \sqrt{f'(\rho)^2 - g'(\rho)^2 + \left(1 - \frac{B^2 R^4}{(\rho^2 + L^2(\rho))^2}\right) (1 + L'^2)}. \quad (4.2)$$

The factor of $2\pi^2$ is just the volume of a unit S^3 , and $\mathcal{N} = \frac{T_7}{g_s} \text{Vol}(\mathbb{R}^4) 2\pi^2$. As the action depends on the ρ -derivatives of A_x and A_t only through the field strength [25], the Euler-Lagrange equations for A_t and A_x demand the existence of two conserved quantities,

$$\delta A_t : D = \frac{\mathcal{N} \rho^3 g'(\rho)}{\sqrt{f'(\rho)^2 - g'(\rho)^2 + \left(1 - \frac{B^2 R^4}{(\rho^2 + L^2(\rho))^2}\right) (1 + L'^2)}}, \quad (4.3)$$

$$\delta A_x : \mathcal{B} = -\frac{\mathcal{N} \rho^3 f'(\rho)}{\sqrt{f'(\rho)^2 - g'(\rho)^2 + \left(1 - \frac{B^2 R^4}{(\rho^2 + L^2(\rho))^2}\right) (1 + L'^2)}}. \quad (4.4)$$

The field theory interpretation of these quantities is given in [25]: D corresponds to a finite baryon number density $\langle J_t \rangle$, and \mathcal{B} to a current in x -direction $\langle J_x \rangle$. Inverting (4.3) and (4.4) yields

$$f'(\rho) = +\mathcal{B} \frac{\sqrt{1 + L'^2(\rho)} \sqrt{1 - \frac{B^2 R^4}{(\rho^2 + L^2(\rho))^2}}}{\sqrt{\mathcal{N}^2 \rho^6 + D^2 - \mathcal{B}^2}}, \quad (4.5)$$

$$g'(\rho) = -D \frac{\sqrt{1 + L'^2(\rho)} \sqrt{1 - \frac{B^2 R^4}{(\rho^2 + L^2(\rho))^2}}}{\sqrt{\mathcal{N}^2 \rho^6 + D^2 - \mathcal{B}^2}}. \quad (4.6)$$

Using these solutions, as in [25] we now perform a Legendre transform eliminating f and g completely from the action and replacing them by the conserved quantities \mathcal{B} and D ,

$$\begin{aligned} \bar{S}_{D7} &= S_{D7} - \int d\rho \left(g'(\rho) \frac{\delta S_{D7}}{\delta g'(\rho)} + f'(\rho) \frac{\delta S_{D7}}{\delta f'(\rho)} \right) \\ &= - \int d\rho \sqrt{(\mathcal{N}^2 \rho^6 + D^2 - \mathcal{B}^2)(1 + L'^2)} \left(1 - \frac{B^2 R^4}{(\rho^2 + L^2(\rho))^2} \right). \end{aligned} \quad (4.7)$$

⁴In fact, for the reality of the DBI action it is enough to introduce the magnetic component $F_{\rho x}$. We however also consider the electric component $F_{\rho t}$, which corresponds to introducing a chemical potential and a finite baryon number density on the brane.

⁵One may check that for the RR four-form potential (2.3), the Chern-Simons part of the D7-brane action only contributes through the gauge field strength components $F_{\hat{a}\hat{b}}$, $\{\hat{a}, \hat{b}\} \in \{\rho, \psi, \beta, \gamma\}$. The coupling to the magnetic dual four-form \tilde{C}_4 vanishes because $P[\tilde{C}_4] = 0$ for our choice of the embedding. Furthermore, we are suppressing here the customary factor of $2\pi\alpha'$ in front of the Faraday tensor. It can easily be restored.

We see that it is possible to obtain an action which is real everywhere by demanding that at the point $\rho_{IR}^2 + L(\rho_{IR})^2 = BR^2$, where the last bracket in the square root of (4.7) changes sign, the first bracket therein should also change sign. This implying a relation between the two conserved quantities and the position where the brane hits the singular shell,

$$\mathcal{B}^2 = \mathcal{N}^2 \rho_{IR}^6 + D^2. \quad (4.8)$$

Reinserting this relation into (4.7), we find

$$\bar{S}'_{D7} = -\mathcal{N} \int d\rho \sqrt{(\rho^6 - \rho_{IR}^6)(1 + L'^2) \left(1 - \frac{B^2 R^4}{(\rho^2 + L^2(\rho))^2}\right)}. \quad (4.9)$$

In the finite temperature AdS-Schwarzschild background (3.1) the corresponding expressions read ($L_{IR} = L(\rho_{IR})$)

$$\omega_{IR}^2 = \rho_{IR}^2 + L_{IR}^2 = \frac{BR^2}{2} + \frac{1}{2} \sqrt{4b^4 + B^2 R^4}, \quad (4.10)$$

$$\mathcal{B}^2 = \frac{(\omega_{IR}^4 - b^4)^2}{(\omega_{IR}^4 + b^4)^2} D^2 + \frac{\mathcal{N}^2 B^2 R^4 (\omega_{IR}^4 + b^4) \rho_{IR}^6}{\omega_{IR}^8}, \quad (4.11)$$

$$\bar{S}'_{D7} = - \int d\rho \sqrt{a \left(\mathcal{N}^2 \left(\rho^6 - \frac{b_{IR} c_{IR}}{bc} \rho_{IR}^6 \right) + D^2 \frac{b - b_{IR}}{bc} \right)},$$

with

$$a = (1 + L'^2) \left(1 + \frac{b^4}{\omega^4}\right)^2 \left(\left(1 - \frac{b^4}{\omega^4}\right)^2 - \frac{B^2 R^4}{\omega^4} \right),$$

$$b = \left(1 - \frac{b^4}{\omega^4}\right)^2 \left(1 + \frac{b^4}{\omega^4}\right), \quad c = \left(1 + \frac{b^4}{\omega^4}\right)^3. \quad (4.12)$$

At finite temperature the singular shell always resides outside the horizon at $\omega_{hor}^2 = b^2$. There is an important difference between the cases of finite and zero temperature: While (4.12) does, after Legendre transformation, explicitly depend on D , the zero temperature action (4.9) does not. Both are, however, real, over the whole range $\rho \in [0, \infty)$ *per constructionem*. The embeddings in the zero temperature case thus will not depend on the baryon number density, but the finite temperature embeddings will: The choice of D at finite temperature influences the asymptotic values of the quark masses for the D7 branes falling into the horizon, i.e. sets an energy scale.

4.1.1 Embeddings

We begin by studying the D7 brane embeddings at zero temperature and with $D = 0$, which are depicted in figure 8. For Minkowski embeddings (depicted in blue), which do not reach the singular shell but flow all the way to $\rho_{IR} = 0$, the gauge field can be turned off consistently: $A_x = A_t = 0$. There also are embeddings which do intersect the singular shell (depicted in green): Some of these flow towards the origin $L = \rho = 0$, i.e. the location of the AdS horizon, while others end in a conical singularity at $\rho = 0$. For the singular shell embeddings, the infrared value ρ_{IR} is given by $\rho_{IR}^2 + L_{IR}^2 = BR^2$, where L_{IR} is the value of L at which they intersect the singular shell.

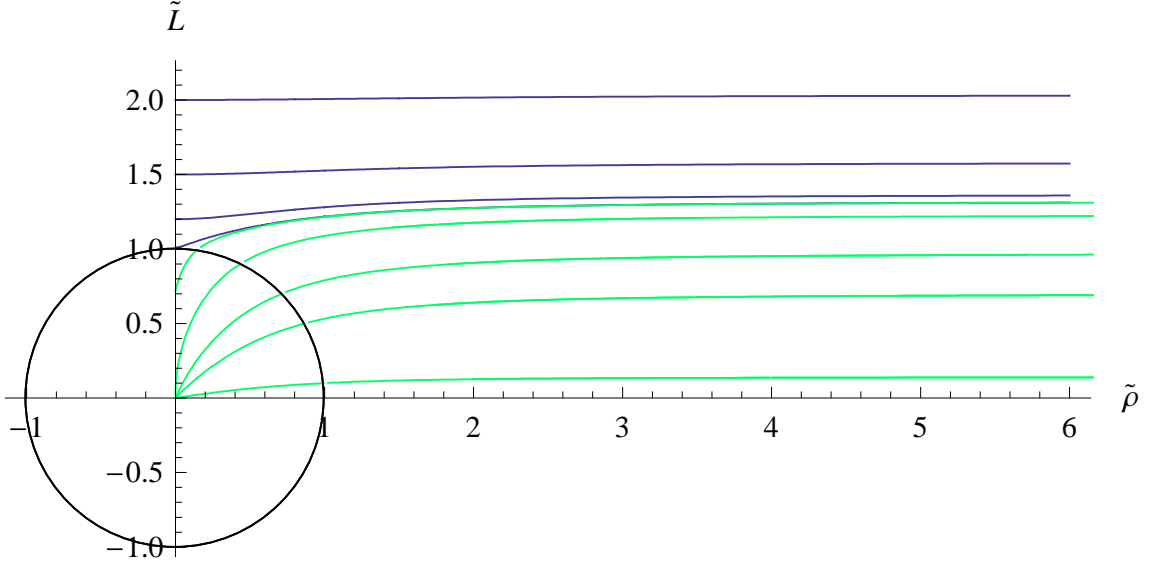


Figure 8: D7 brane embeddings for the electric B field at zero temperature. The blue curves are Minkowski embeddings, while the green ones reach the singular shell. The singular shell attracts the D7 brane probes as in the finite temperature case, and bends them towards the origin.

The action (4.9) is real everywhere, and reduces to (2.5) with the lower sign for the Minkowski embeddings, for which $\rho_{IR} = 0$. The Euler-Lagrange equation for $L(\rho)$ as derived from (4.9) reads

$$\partial_\rho \left(\frac{\sqrt{\rho^6 - \rho_{IR}^6} L' \sqrt{1 - \frac{B^2 R^4}{(\rho^2 + L^2)^2}}}{\sqrt{1 + L'^2}} \right) - \frac{2B^2 R^4 L \sqrt{\rho^6 - \rho_{IR}^6} \sqrt{1 + L'^2}}{(\rho^2 + L^2)^3 \sqrt{1 - \frac{B^2 R^4}{(\rho^2 + L^2)^2}}} = 0. \quad (4.13)$$

In practice we obtain the Minkowski embeddings by shooting out from the L-axis to infinity, while the singular shell embeddings are obtained by shooting inwards and outwards starting from the shell, with the condition that the embedding crosses the shell perpendicularly⁶.

We extract the UV asymptotic values of \tilde{m} for each flow according to (2.9). In figure 9 we plot the condensate \tilde{c} as a function of the reduced quark mass \tilde{m} . The blue curve again corresponds to the Minkowski embeddings, while the green curve is for the embeddings flowing into the shell of vanishing action. There is a first order phase transition at the point where both curves join. This region is shown in detail in figure 10, where we find a three-fold degeneracy for a range of masses between about $\tilde{m} = 1.316$ and $\tilde{m} = 1.319$, in exact analogy to the finite temperature case [8], where \tilde{m} is defined as in (2.9). The exact point of the phase transition can be found by the equal area method:⁷ As $\tilde{c}(\tilde{m})$ in the holographic context is proportional to the first derivative of the free energy, the area below this curve is proportional to the free energy itself. In a region with several possible

⁶In fact, as we checked, different crossing angles affect the UV and IR behaviour only minimally.

⁷See references [3, 29] for the application of the equal area law to such situations.

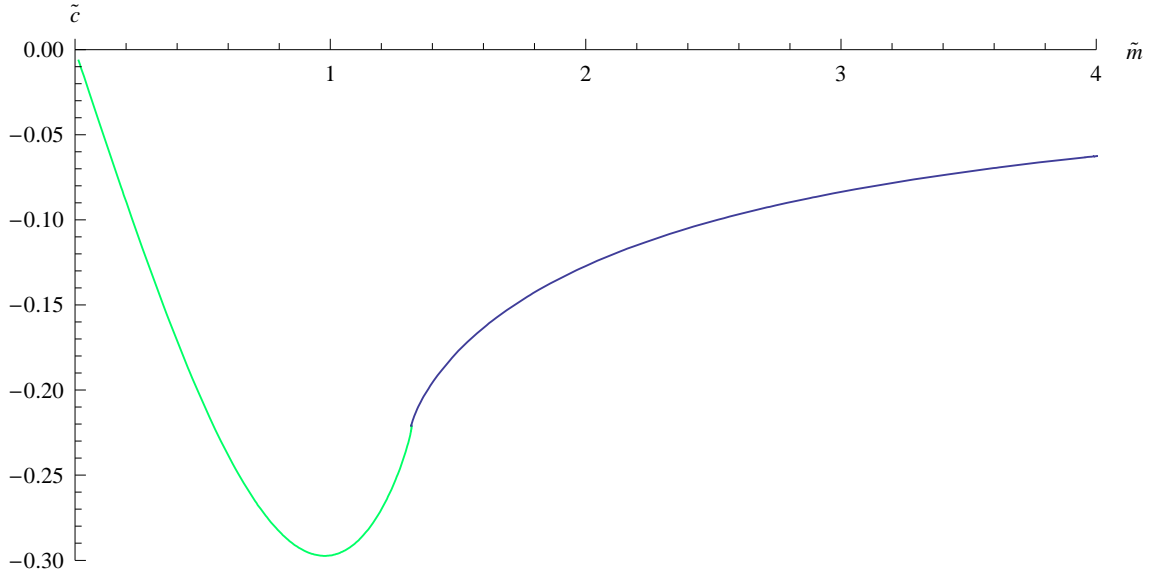


Figure 9: $\tilde{c}(\tilde{m})$ for the embeddings in the electric zero temperature case. The blue line corresponds to the Minkowski solutions, and the green line to those flowing into the shell.

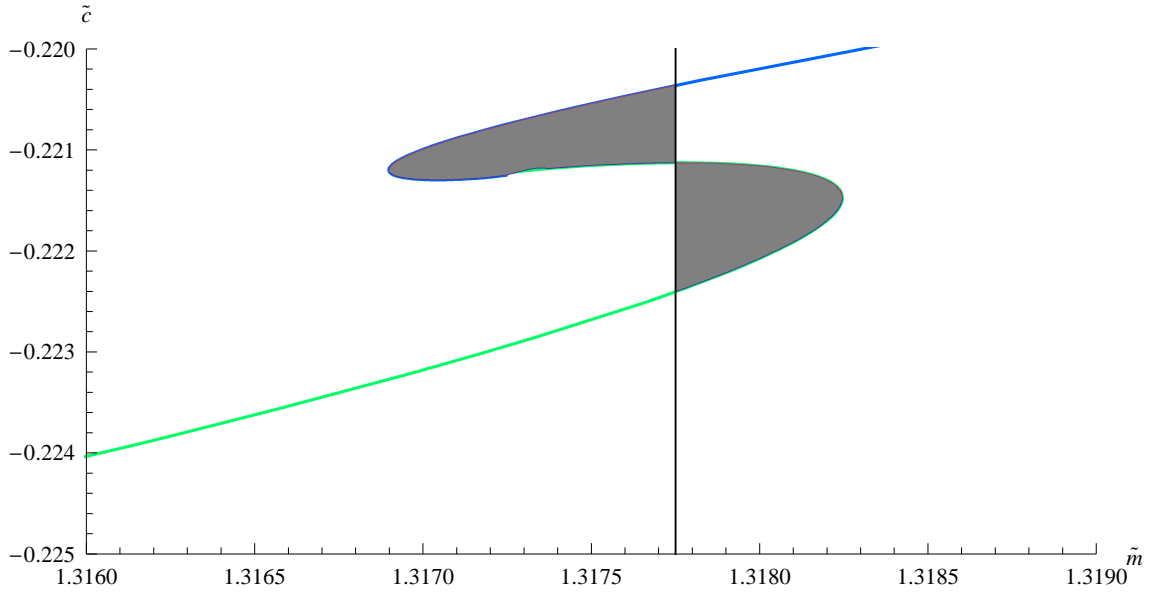


Figure 10: $\tilde{c}(\tilde{m})$ for both physical and nonphysical embeddings in the region $1.317 \leq \tilde{m} \leq 1.322$. The “S”-shaped bend indicates a first order phase transition at $\tilde{m} \approx 1.31775$, found by the “equal area law” (see text).

embeddings, the phase transition then occurs where the difference of the free energies of the two phases has a zero, i.e. where the areas below the $c(m)$ curve are equal. We find that below a reduced quark mass of $\tilde{m} = 1.31775$, the solutions flowing into the shell of

vanishing action become energetically favoured.

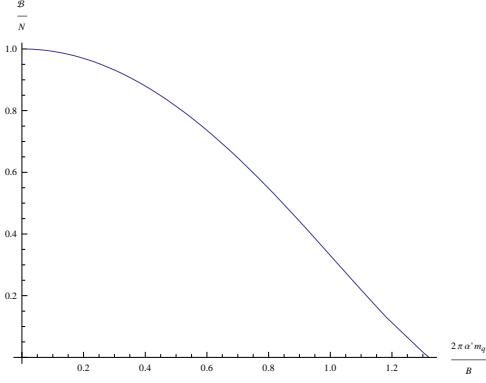


Figure 11: Induced baryon number current over reduced quark mass for zero temperature and baryon density.

The induced baryon number current $\langle J_x \rangle = \mathcal{B}$, which is shown in figure 11, shows an interesting behaviour too: For a fixed value of the B field it decreases with growing quark mass until the phase transition point is reached, where the Minkowski embeddings, which have zero induced current, smoothly take over. Note that this plot also includes the singular shell embeddings, whose physical fate still needs to be decided, cf. section 5. In any case, a kind of threshold for the induced current at zero temperature and baryon density is expected, as vacuum pair production should be impossible for high enough quark masses.

4.1.2 Meson spectrum

We now turn to the calculation of the meson spectrum in the presence of the electric Kalb-Ramond field at zero temperature. Up to small modifications, the calculation is very similar to the one performed for the magnetic case in [23]. For the fluctuations we use the ansatz

$$\begin{aligned} L(\rho) &= L_0(\rho), \\ \Phi &= \phi = h(\rho)e^{ik_0 t - ik_1 x_1} Y_l(S^3), \end{aligned} \quad (4.14)$$

for which we show the decoupling from the L - and gauge field fluctuations on Minkowski embeddings in appendix B. Here L_0 is the embedding obtained from the equation of motion (4.13). Note that in (4.14) we now consider a meson in the (t, x_1) plane, as opposed to the magnetic case (3.6) where the meson is in the (x_2, x_3) plane. Linearising the D7-brane action in an analogous way to the calculation performed in [23], we obtain the equation of motion for the excitations ϕ ,

$$\frac{1}{g} \partial_\rho \left(\frac{g L_0^2 \partial_\rho h(\rho)}{1 + L_0'^2} \right) - \frac{L_0^2 l(l+2)}{\rho^2} h(\rho) + \frac{R^4 L_0^2 M_{01}^2}{(\rho^2 + L_0^2)^2 - R^4 B^2} h(\rho) = 0. \quad (4.15)$$

Here $M_{01}^2 = k_0^2 - k_1^2$ is the meson mass and $g = \rho^3 \sqrt{1 + L_0'^2} \sqrt{1 - \frac{B^2 R^4}{(\rho^2 + L_0^2)^2}}$. We consider only s-wave fluctuations, corresponding to pseudoscalar mesons ($l = 0$), and calculate the spectrum for Minkowski embeddings. The results for $BR^2 = 1$ are displayed in Figure 12. The dashed lines in figure 12 show the analytic AdS solutions, $\tilde{M} = 2\tilde{m}\sqrt{(n+1)(n+2)}$. The behaviour shown in figure 12 is consistent with intuitive expectations: For large reduced quark mass \tilde{m} the D-branes do not feel the forces exerted by the singular shell (see figure 8) and thus are approximately flat, as dictated by supersymmetry of the pure AdS setting [1].

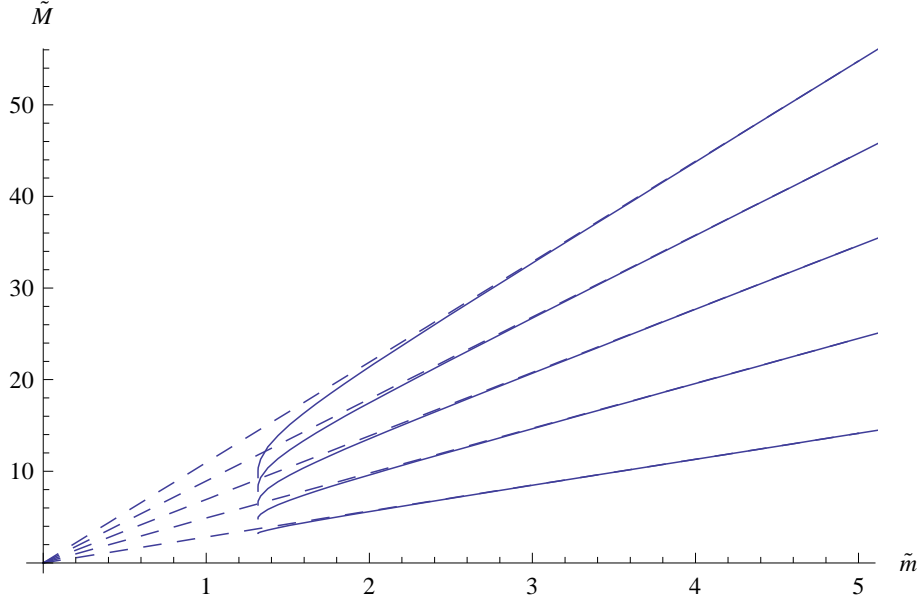


Figure 12: First five meson states in the electric ansatz background for the Minkowski embeddings. $\tilde{M} = \frac{R}{\sqrt{B}} M_{01}$, $\tilde{m} = \frac{m_q 2\pi\alpha'}{\sqrt{B}R}$.

Note that in contrast to the effect of a magnetic Kalb-Ramond field, the mesons in the presence of the electric field are lighter than without applied field. The electric field thus reduces the binding energy. For the embeddings ending inside the shell, we expect the mesons to destabilize through a mechanism similar to ionization, in analogy to the black hole scenario. We leave this for further study.

4.2 Stark effect

For weak external electric fields at zero temperature, we now analytically calculate the meson mass shift of the $n = l = 0$ state, which in the corresponding region of large mass is the lightest meson in figure 12, and thus the ground state. For this purpose, we use a technique similar to first order perturbation theory familiar from quantum mechanics, which in this context was suggested to us by Derek Teaney [42].

We start by looking at the perturbation exerted by the electric field on a Minkowski embedding, i.e. an embedding that has high enough quark mass such that it does not reach the singular shell. Its fluctuation spectrum is then discrete, such that the meson masses are well-defined. To expand the equation for the Φ fluctuations (4.15) to lowest non-trivial order in the electric field, which in fact is $\mathcal{O}(B^2)$, we use the following perturbative solution for the brane embedding to $\mathcal{O}(B^2)$,

$$L = m - \frac{B^2 R^4}{4m(\rho^2 + m^2)}. \quad (4.16)$$

This result is easily obtained by expanding the embedding equation (4.13) up to second order in B . The $\mathcal{O}(B)$ term would not satisfy the Minkowski embedding boundary condition

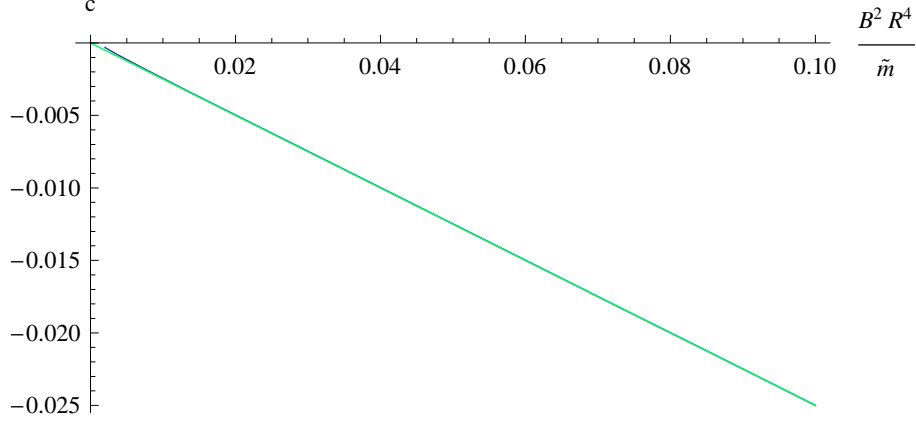


Figure 13: The condensate as a function of $\frac{B^2 R^4}{m}$, both numerically (dark curve) and in the weak field approximation (4.17) (green curve). Both curves have a gradient of -4.

$L'(0) = 0$ and thus has to vanish. By comparing (4.16) with (2.7) we find that the condensate at small field strength or equivalently large quark mass is

$$c(m) = -\frac{B^2 R^4}{4m}. \quad (4.17)$$

Figure 13 shows the quark condensate as a function of $\frac{B^2 R^4}{m}$. The dark curve corresponds to numerical data, while the light green curve is the weak field result (4.17). Both curves coincide to high precision, and both have a slope of minus four, thus validating (4.17). The slight mismatch near the origin, i.e. in the small B or large m region where the approximation should hold very well, is due to numerical instabilities.

Using (4.16) as well as the identities (A.1)-(A.3) in appendix A, the equation for the Φ -fluctuations (4.15) up to second order in B reads

$$\rho^{-3} \partial_\rho (\rho^3 h'(\rho)) + \frac{(M_0^2 + \delta(M^2)) R^4 h(\rho)}{(\rho^2 + m^2)^2} = \frac{B^2 R^4}{2m^2} \left[-\frac{M_0^2 R^4 (3m^2 - \rho^2) h(\rho)}{(\rho^2 + m^2)^4} - \frac{4\rho m^2 h'(\rho)}{(\rho^2 + m^2)^3} + \rho^{-3} \partial_\rho \left(\frac{\rho^3 h'(\rho)}{\rho^2 + m^2} \right) \right]. \quad (4.18)$$

Here we split the exact mass of the ground state $M^2 = M_0^2 + \delta(M^2)$ into the unperturbed AdS piece $M_0^2 = 8m^2/R^4$ and a lowest order correction. It is convenient to introduce dimensionless quantities⁸ $\tilde{\rho} = \rho/m$, $\tilde{M}^2 = R^4 M^2/m^2$ and $\tilde{B}^2 = B^2 R^4/(2m^4)$. In these units and after multiplying by $\tilde{\rho}^3 m^2$, eq. (4.18) becomes

$$\partial_{\tilde{\rho}} (\tilde{\rho}^3 h'(\tilde{\rho})) + W(\tilde{\rho})(\tilde{M}_0^2 + \delta(\tilde{M}^2))h(\tilde{\rho}) = \tilde{B}^2 \left[-\frac{\tilde{M}_0^2 W(\tilde{\rho})(3 - \tilde{\rho}^2)h(\tilde{\rho})}{(\tilde{\rho}^2 + 1)^2} - \frac{4\tilde{\rho} W(\tilde{\rho})h'(\tilde{\rho})}{\tilde{\rho}^2 + 1} + \partial_{\tilde{\rho}} (W(\tilde{\rho})h'(\tilde{\rho})(\tilde{\rho}^2 + 1)) \right], \quad (4.19)$$

⁸Note $m = m_q/(2\pi\alpha')$ has dimension length.

where we defined the weight function $W(\tilde{\rho}) = \frac{\tilde{\rho}^3}{(1+\tilde{\rho}^2)^2}$. We immediately see that the lowest order shift in masses will be proportional to \tilde{B}^2 . We now use a strategy similar to first order perturbation theory in quantum mechanics: The fluctuation equation for the pure $AdS_5 \times S^5$ case

$$\partial_{\tilde{\rho}} (\tilde{\rho}^3 h'(\tilde{\rho})) + W(\tilde{\rho}) \tilde{M}_n^2 h(\tilde{\rho}) = 0,$$

is a Sturm-Liouville problem. This implies [43] that its normalizable eigenfunctions

$$h_n(\tilde{\rho}) = c_n (1 + \tilde{\rho}^2)^{-(n+1)} {}_2F_1(-(n+1), -n, 2, -\tilde{\rho}^2), \quad \tilde{M}_n^2 = 4(n+1)(n+2), \quad (4.20)$$

which have been found in [44], can be used to define an orthonormal basis of functions $f_n(\tilde{\rho})$ on the interval $\tilde{\rho} \in [0, \infty)$ w.r.t to the inner product

$$(f, g) = \int_0^\infty d\tilde{\rho} W(\tilde{\rho}) f(\tilde{\rho}) g(\tilde{\rho}). \quad (4.21)$$

Here ${}_2F_1(a, b, c, z)$ is the Gauss hypergeometric function. Let $\{f_n, n = 0, 1, \dots\}$ be such a set, satisfying orthonormality

$$(f_n, f_m) = \delta_{nm}, \quad (4.22)$$

and let us normalize the ground state wave function $h_0(\tilde{\rho})$ by choosing the coefficient $c_0 = \sqrt{12}$ such that $f_0 = h_0$. In what follows we will only need the explicit form of this ground state wave function⁹

$$f_0(\tilde{\rho}) = \frac{\sqrt{12}}{1 + \tilde{\rho}^2}, \quad (4.23)$$

and the fact that the above orthonormal basis exists [43]. The idea is now that the normalized ground state wave function f_0 only gets perturbed by a small amount, which is encoded in the ansatz $h(\tilde{\rho}) = a_0 f_0 + \sum_{n>0} a_n f_n \rho$, where $a_0 = 1 + \mathcal{O}(\tilde{B}^4)$ and $a_n = \mathcal{O}(\tilde{B}^2), n > 0$.

Plugging this ansatz into (4.19), keeping only terms $\mathcal{O}(\tilde{B}^2)$ and using that the f_n satisfy the equation¹⁰

$$\partial_{\tilde{\rho}} (\tilde{\rho}^3 f_n) = -\tilde{M}_n'^2 f_n W,$$

we find

$$\begin{aligned} \sum_{n>0} a_n f_n (\tilde{M}_n'^2 - \tilde{M}_0^2) W + \delta(\tilde{M}^2) W f_0 = \\ \tilde{B}^2 \left[-\frac{\tilde{M}_0^2 W f_0 (3 - \tilde{\rho}^2)}{(1 + \tilde{\rho}^2)^2} - \frac{4W \tilde{\rho} f_0'}{1 + \tilde{\rho}^2} + \partial_{\tilde{\rho}} (W(\tilde{\rho}) f_0'(\tilde{\rho}) (\tilde{\rho}^2 + 1)) \right]. \end{aligned} \quad (4.24)$$

⁹Note that ${}_2F_1(-1, 0, 2, -\tilde{\rho}^2) = 1$.

¹⁰Note that $\tilde{M}_n'^2 \neq \tilde{M}_n^2$ in general, but $\tilde{M}_0'^2 = \tilde{M}_0^2$ because of our choice $f_0 = h_0$.

Now multiplying with f_0 and integrating over $\tilde{\rho}$ yields, after using orthonormality relation (4.22), an expression for the mass shift

$$\delta(\tilde{M}^2) = \tilde{B}^2 \left[\underbrace{-\tilde{M}_0^2 \left(f_0, f_0 \frac{3-\tilde{\rho}^2}{(1+\tilde{\rho}^2)^2} \right)}_{I_1} \underbrace{-4 \left(f_0, \frac{\tilde{\rho} f'_0}{1+\tilde{\rho}^2} \right)}_{I_2} + \underbrace{\left(\frac{f_0}{W}, \partial_\rho (W(\tilde{\rho}) f'_0(\tilde{\rho}) (\tilde{\rho}^2 + 1)) \right)}_{I_3} \right]. \quad (4.25)$$

The individual contributions are ($\tilde{M}_0^2 = 8$)

$$\begin{aligned} I_1 &= -96 \int_0^\infty d\rho \frac{\rho^3(3-\rho^2)}{(1+\rho^2)^6} = -\frac{28}{5}, \\ I_2 &= -48 \int_0^\infty d\rho \frac{\rho^4}{(1+\rho^2)^4} \left(\frac{1}{(1+\rho^2)} \right)' = 96 \int_0^\infty d\rho \frac{\rho^5}{(1+\rho^2)^6} = \frac{8}{5}, \\ I_3 &= -24 \int_0^\infty \frac{d\rho}{(1+\rho^2)} \left(\frac{\rho^4}{(1+\rho^2)^3} \right)' = -48 \int_0^\infty d\rho \frac{\rho^3(2-\rho^2)}{(1+\rho^2)^5} = -2. \end{aligned}$$

In dimensionless units, the mass of the ground state is thus shifted by

$$\delta(\tilde{M}^2) = -6\tilde{B}^2 = -3 \frac{B^2 R^4}{m^4}. \quad (4.26)$$

Reinstating physical units yields

$$\delta M = -\frac{3}{4\sqrt{2}} \frac{B^2 R^2}{m^3} = -\frac{3}{16\sqrt{2}\pi^{5/2}} \frac{B^2 \sqrt{\lambda}}{\alpha'^2 m_q^3} \approx -0.00758 \frac{B^2 \sqrt{\lambda}}{\alpha'^2 m_q^3}. \quad (4.27)$$

There are several points to mention for this result: First, it has the expected B^2 behaviour of the second order Stark effect. Second, it has the correct sign, i.e. the mass of the ground state is lowered compared to the pure AdS case (c.f. figure 12). Furthermore, by introducing physical units for the B field $\bar{B} = B/2\pi\alpha'$, which is of dimension mass squared, the result becomes independent of α' and is thus finite in the $\alpha' \rightarrow 0$ limit,

$$\delta M \approx -0.00758 \frac{\bar{B}^2}{m_q^3} 4\pi^2 \sqrt{\lambda}. \quad (4.28)$$

The dependence on the 't Hooft coupling λ is also easily understood: As the meson masses themselves are proportional to $1/\sqrt{\lambda}$ [44] (c.f. e.g. (4.20) and note $R^2 = \sqrt{4\pi\lambda\alpha'}$), the combination \bar{B}^2/m_q^3 must scale like λ^{-1} , i.e. must be small in the 't Hooft limit $N \rightarrow \infty$ with $\lambda = g_s N = \text{const.} \gg 1$. This means just that the small \bar{B} expansion is valid if either the physical B field \bar{B} is small or the quark mass m_q is large.

Let us now compare this analytical calculation of the Stark effect with the numerical data displayed in figure 12. In the limit of large quark mass \tilde{m} , we study the difference between the AdS meson spectrum and the value of \tilde{M} . Numerically we find that ¹¹

$$\delta\tilde{M} = \tilde{M} - \tilde{M}_{AdS} = -\frac{0.54R^2}{\tilde{m}^3}. \quad (4.29)$$

Performing the appropriate rescaling of \tilde{M} and \tilde{m} to reintroduce B we find that

$$\delta M = -\frac{0.54B^2R^2}{m^3}.$$

From equation (4.27) we find

$$\delta M = -\frac{0.53B^2R^2}{m^3}, \quad (4.31)$$

in very good agreement with the numerical calculation. The discrepancy is likely to come from both numerical errors and higher order corrections in the expansion around small B (large m). Table 1 shows the coefficients c_n and α_n in the mass shift

$$\delta M = -c_n \frac{B^2R^2}{m^{\alpha_n}} \quad (4.32)$$

as obtained by fitting (4.32) to the numerical result for the meson masses displayed in figure 12, also for the higher modes $n \geq 1$. Keeping in mind that according to our experience, the numerical errors get larger for higher states (although we can not specify the error quantitatively), there is a chance that α_n is n -independent with a value of three, as can be expected on dimensional grounds by requiring the mass shift to be proportional to the dimensionful Kalb-Ramond field \bar{B}^2 and simultaneously independent of α' .

4.3 Electric Kalb-Ramond field at finite temperature

We conclude this section by commenting on the embeddings in the finite temperature AdS-Schwarzschild background with electric field, which we obtain numerically from the action (4.12). Since we are introducing baryon number density through the D7 brane gauge field, we have to distinguish between embeddings for zero and finite density, as smooth Minkowski embeddings are only consistent for vanishing density [12]. Note that considering finite densities is the more general case: For ensuring a regular DBI action at the singular shell, $D = 0$ would suffice to satisfy equation (4.11).

Figure 14 shows embeddings calculated for different strengths of the B-field, and vanishing baryon density $D = 0$. Since at zero baryon density both Minkowski and singular shell embeddings are consistent (cf. figure 8), a well-defined zero temperature limit in the canonical ensemble reproducing figure 8 is possible for $D = 0$ only (see the discussion in section 5). As can be seen from figure 14, in contrast to finite baryon number density, the black hole embeddings cover only a finite range of asymptotic quark mass up to a maximal value. Above this mass, which depends on the B field through $\tilde{m} = (1.27 \pm 0.03)\sqrt{BR^2 + \sqrt{4b^4 + B^2R^4}}/\sqrt{2}$, Minkowski embeddings take over. This now

¹¹Note that in the units of figure 12, B is scaled to $B = 1$.

Level n	c_n	α_n
0	0.54	3.0
1	1.80	3.1
2	3.62	3.2
3	7.85	3.4
4	8.85	3.4

Table 1: Fitted coefficients of the Stark shift, where $\delta M_n = -\frac{c_n B^2 R^2}{m^{\alpha_n}}$.

$$(4.30)$$

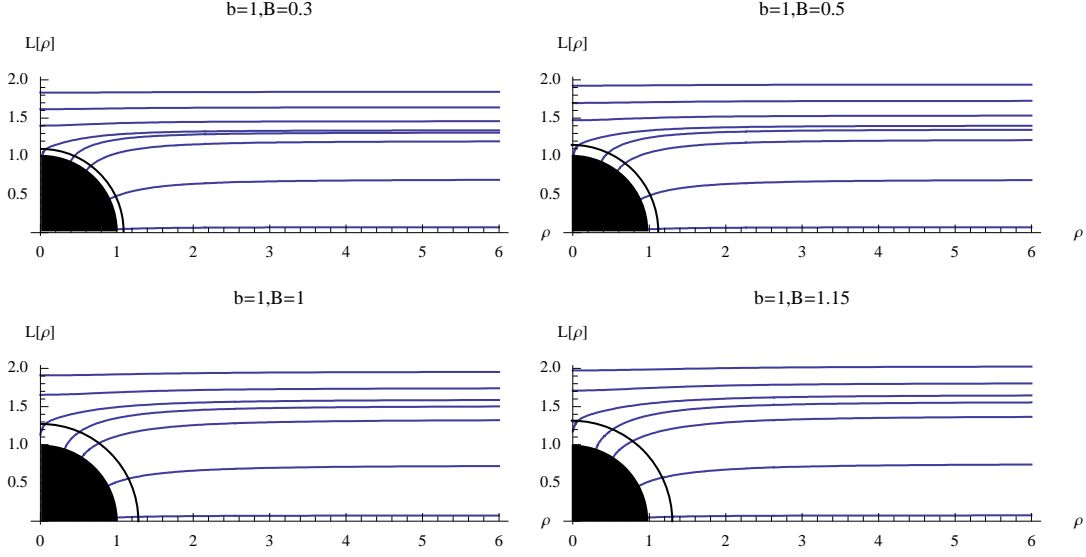


Figure 14: Minkowski and singular shell embeddings for the electric case at finite temperature and zero baryon number density $D = 0$.

allows for a well-defined zero temperature limit. Lowering the temperature, the black hole horizon shrinks to the extremal AdS horizon at $\rho = L = 0$, where the black hole embeddings then end. The corresponding chiral condensate, in particular its dependence on the field strength, on the temperature and on the quark mass, was calculated in [30].

Figures 15 and 16 show black hole embeddings calculated for a baryon number density of $D = 10$ and $D = 20$, respectively. For comparison we also included Minkowski embeddings which, as we know very well, can only coexist with black hole embeddings at finite baryon number density in a grand canonical ensemble [13], where the baryon chemical potential is fixed instead of the number density (cf. also section 5). The black hole embeddings pass through the shell of vanishing action smoothly and reach the black hole horizon. We observe that black hole embeddings at finite baryon number density can cover the whole range of asymptotic quark masses, a fact already noted without external electric fields in [12]. Comparing the two figures 15 and 16, we find the effect of changing the baryon number density D as given by (4.3): In both figures, the Minkowski and black hole embeddings were calculated for the same values of the infrared boundary condition $L(\rho_{IR}) = L_{IR}$. The green black hole embeddings are sensitive to the value of D : For a given infrared boundary condition, they reach larger asymptotic quark masses $L(\infty)$ for larger D . Thus the scaling of D corresponds to a dilation of the energy scale. Note that this scaling effect is also present for black hole embeddings in the canonical ensemble at zero external electric field, c.f. e.g. figure 4 in [12].

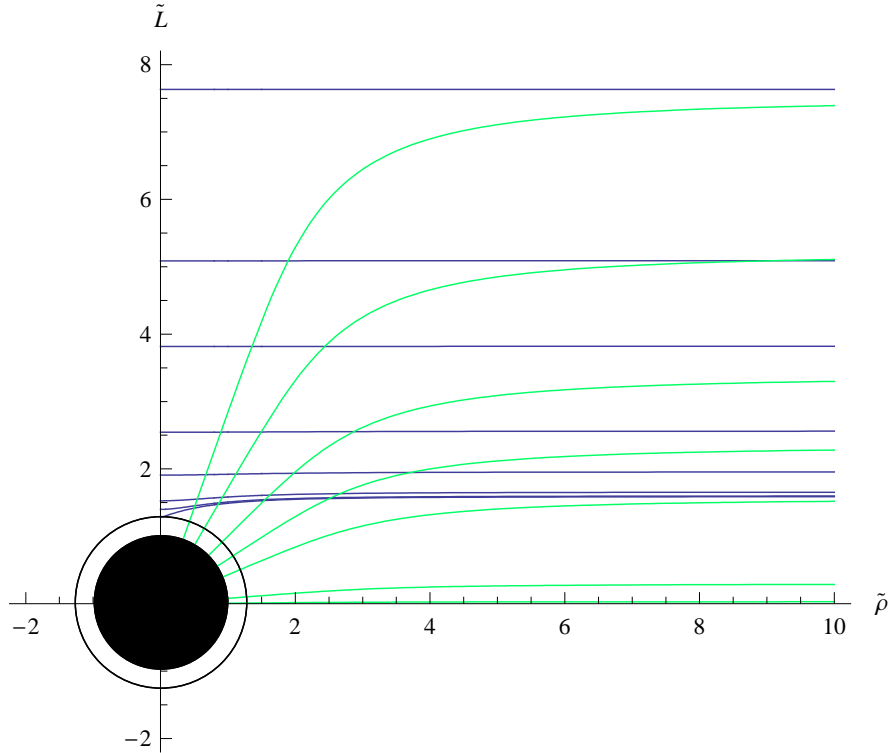


Figure 15: Minkowski ($b = B = R = 1$, $D = 0$) and black hole embeddings for the electric case at finite temperature ($b = B = R = 1$, $D = 10$). Note that both types embeddings can only exist simultaneously in the grand canonical ensemble [13].

5. Conclusions and Outlook

The magnetic (spatial-spatial) and electric (temporal-spatial) external B fields in the directions parallel to the boundary have quite different effects on D7 probe brane embeddings. In the magnetic case there is a repulsion, such that even at finite temperature spontaneous chiral symmetry breaking occurs. The magnetic field has a confining effect on the mesons.

In the electric case there is a singular shell on which the DBI action vanishes. This shell has an attractive effect on the embeddings, which may be interpreted as ionization. A gauge field has to be switched on to ensure a regular action inside the shell. The full stability analysis of this scenario is delicate, as strings in electric fields are known to display instabilities, and we leave this analysis for further study here.

Let us, however, comment on the question of the thermodynamical ensemble considered in the electric case. As shown in [12], switching on a gauge field A_t corresponds to including baryon number density and a baryon chemical potential into the thermodynamics of the dual gauge theory. The canonical ensemble is then characterized by a fixed number density and a varying chemical potential, while in the grand canonical ensemble the chemical potential is held fixed [47]. Furthermore, Minkowski embeddings which close off smoothly at $\rho = 0$ are only consistent for vanishing baryon number density: A nonvanishing baryon number density would correspond to strings creating a cusp at $\rho = 0$ on the brane while

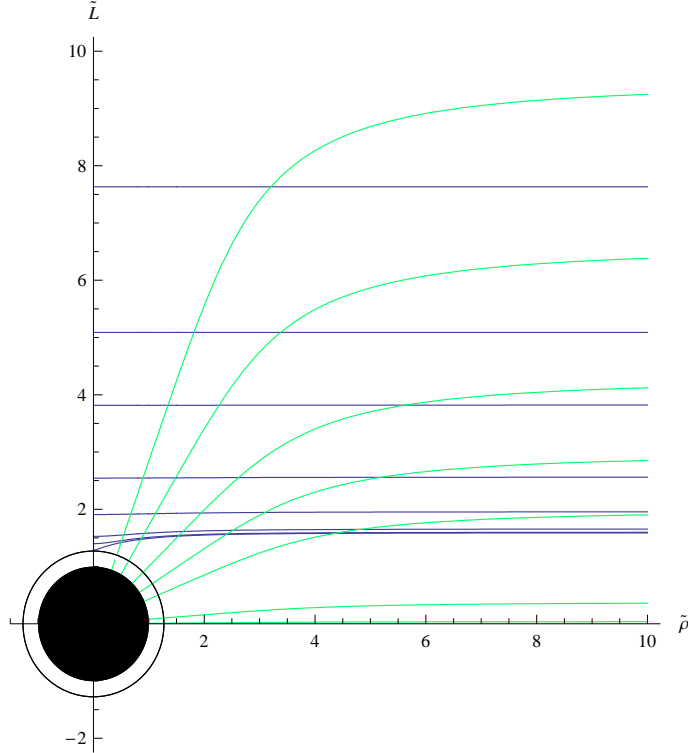


Figure 16: Minkowski ($b = B = R = 1$, $D = 0$) and black hole embeddings for the electric case at finite temperature ($b = B = R = 1$, $D = 20$). Note that both types embeddings can only exist simultaneously in the grand canonical ensemble [13].

stretching down to the black hole horizon [12], or to the AdS horizon in the zero temperature limit. Thus, as we interpret our results with fixed number density D as in [25], we are naturally considering the system in the canonical ensemble.

For vanishing baryon density $D = 0$, when Minkowski embeddings are consistent, the embeddings which reach the singular shell would necessarily have vanishing baryon number density too. However, due to eq. (4.11), these embeddings correspond to a nonzero induced baryon number current $\langle J_x \rangle = \mathcal{B}$. This describes the situation after meson melting, where the quarks and antiquarks are accelerated by the applied external Kalb-Ramond field. This is equivalent to vacuum pair production of baryon number charge by thermal effects and by the applied external field. This interpretation coincides with the result of [25] that the baryon number conductivity is finite even in the $n_q \rightarrow 0$, $T \rightarrow 0$ limit.

At zero baryon number density, figures 8 and 14 show that above a certain asymptotic quark mass, the embeddings do not reach the singular shell any more. We then expect the dissociation phase transition to happen between a singular shell embedding and a Minkowski one. This again coincides with the necessity to ascribe a vanishing baryon number density to the singular shell embeddings in the canonical ensemble, as the dissociation of a meson, i.e. a quark-antiquark pair, will not create finite quark number densities¹². In the zero temperature limit, the black hole embeddings end at the point $L = \rho = 0$ (see

¹²The quark and baryon number densities are related by a factor of $n_q = N_c n_b$.

figure 8). This is where the extremal black hole, i.e. the D3-brane horizon sits.

As mentioned before, for finite temperature and nonvanishing baryon density there exist only black hole embeddings in the canonical ensemble (cf. figure 15 and 16). In this case, we expect the dissociation phase transition to occur between two black hole embeddings at least for sufficiently small electric field, where the singular shell is near the horizon and the physics are continuously related to the zero-field case [12].

From the above, we therefore think that an interesting future task is to explore the phase diagram for finite external electric field in the grand canonical ensemble. We expected that Minkowski embeddings might play a role for the dissociation transition at finite temperature similar to the situation described in [47], and that the dissociation of the mesons at high temperatures, or equivalently at small quark masses, could lead to nonzero baryon number densities due to the fixed chemical potential. Note, however, that for finite electric field the application of equilibrium thermodynamics is justified only in the large N_c -limit with $N_f/N_c \rightarrow 0$. In this case, the $\mathcal{N} = 4$ plasma can absorb an infinite amount of energy from the $\mathcal{N} = 2$ baryon number charge carriers (see the conclusions of [25] for details).

The results for the electric Kalb-Ramond field obtained in this paper, come, however, with an open question which should be answered in future work: It remains to analyse whether the conically singular embeddings, whose presence was noticed first in [30], and are also seen in our results, most easily in figure 8, are physical or not. These embeddings occur in the intermediate quark mass range between black hole and Minkowski embeddings. In order to be physical, for instance describing a new intermediary phase of melting mesons in the presence of an external $U(1)$ field, they have to be in a force-balanced state of the D7 brane with strings stretching from the cusp to the horizon. For vanishing B field this situation was analyzed in [12] (around eq. (2.40) there), with the result that such static configurations do not exist. The calculation in [12] relies on the fact that, in the region $\rho \approx 0$, the Legendre-transformed D7-brane action reduces to an action for a density n_q of Nambu-Goto strings smeared in the Minkowski directions and stretching along the L-axis from the black hole horizon to the cusp. In our case, in the same limit, eq. (4.12) becomes¹³

$$\bar{L}'_{D7} \simeq D \sqrt{(g_{tt}(r) - g_{tt}(r_{IR})) \left(1 - \frac{B^2}{g_{tt}(r)g_{xx}(r)}\right) (g_{\rho\rho}(r) + g_{\theta\theta}(r)(\partial_r\theta)^2)}. \quad (5.1)$$

Without the B^2 -term in the square root, this would reduce to a Nambu-Goto type action for strings smeared in the Minkowski directions with density D. It might, however, be possible that the strings get dragged along in the x-direction by the B field, and thus a trailing string dragged through the plasma could be attached at the cusp. Also stringy α' -corrections to the DBI action [48] might resolve the conical singularity in the embedding.

Generically, also from the field theory perspective, an instability is expected in the electric case, since turning on an external electric Kalb-Ramond field also requires the presence of a non-zero gauge field background corresponding to a non-vanishing baryon number density and baryon chemical potential μ . It is known for supersymmetric theories,

¹³Note the change of coordinates $L = r \cos \theta$, $\rho = r \sin \theta$.

which involve scalars, that this leads to an upside-down potential of the form [45]

$$V(\phi) = -\mu^2 |\phi|^2, \quad (5.2)$$

which will, in the end, lead to Bose-Einstein condensation of the scalars. For an isospin chemical potential, this instability was reproduced in the holographic context in [46]. Also in the study of baryon chemical potentials, thermodynamical instabilities of D7 brane embeddings at which tachyonic meson modes appear have been found [12, 13]. These latter instabilities are of a more intricate structure, since they are confined to particular regions of the phase diagram.

The detailed structure of the phase diagram for the electric external field is thus very subtle. It will be interesting to study it further, in particular in the light of the very recent work [17, 47]. Some new results in this direction are presented in [30].

Acknowledgments

We are grateful to Tameem Albash, Paolo Aschieri, Luzi Bergamin, José Edelstein, Nick Evans, Veselin Filev, Johannes Große, Daniel Grumiller, Clifford Johnson, Matthias Kaminski, Paul Koerber, Arnab Kundu, Javier Mas, Jeong-Hyuck Park, Felix Rust, Derek Teaney and Maxim Zabzine for discussions. J. E. is grateful to the Isaac Newton Institute in Cambridge, England, for hospitality during part of this project. R. M. thanks the Erwin-Schrödinger-Institute in Vienna for its hospitality. This work was supported in part by the Cluster of Excellence “Origin and Structure of the Universe”.

A. Some useful expansion formulae

To expand eq. (4.15) while calculating the Stark shift, the following identities which hold up to $\mathcal{O}(B^2)$ are useful:

$$g = \rho^3 \sqrt{1 + L'^2} \sqrt{1 - \frac{B^2 R^4}{(\rho^2 + L^2)^2}} \simeq \rho^3 \left(1 - \frac{B^2 R^4}{2(\rho^2 + m^2)^2} \right), \quad (A.1)$$

$$g^{-1} \simeq \rho^{-3} \left(1 + \frac{B^2 R^4}{2(\rho^2 + m^2)^2} \right), \quad (A.2)$$

$$[(\rho^2 + L^2)^2 - B^2 R^4]^{-1} \simeq (\rho^2 + m^2)^{-2} \left(1 + \frac{B^2 R^4}{(\rho^2 + m^2)^2} \right). \quad (A.3)$$

B. Decoupling of Φ -fluctuations

In this appendix we show that for the magnetic and electric Kalb-Ramond field (2.4), both at finite and zero temperature, the L - and gauge field fluctuations can be decoupled from the Φ -fluctuations and consistently set to zero by the respective ansätze (3.6) and (4.14). For the electric case, as we will show, this holds only for the Minkowski embeddings,

which have both zero baryon number density and current, i.e. for a trivial gauge field background. For a nontrivial gauge field background, like the one which renders the singular shell embeddings consistent, this decoupling will only be possible if the Φ -fluctuations do not depend on the Minkowski coordinates at all, $\phi = \phi(\rho)$. The calculation follows [23].

To show the decoupling, we have to verify that in the part of the action quadratic in the fluctuations no couplings of χ and A to ϕ appear. We take the embedding fluctuations to be $L = L_0(\rho) + \chi$, $\Phi = \phi$, where $L_0(\rho)$ is the embedding of the D7 brane into the appropriate background. For now, let us assume a trivial gauge background $F = 0$ on the brane, such that the gauge field A is a pure fluctuation. For a diagonal background metric $G_{MN}(\rho, L) = \text{diag}(-G_{tt}, G_{xx}, G_{yy}, G_{zz}, G_{\rho\rho}, G_{\eta\eta}, G_{\xi_1\xi_1}, G_{\xi_2\xi_2}, G_{LL}, G_{\Phi\Phi})$ not depending on Φ and the magnetic ansatz (2.4), the pull-back of metric and B field can be split into an embedding part, a part linear and a part quadratic in the fluctuations:

$$E_{ab} = P[G + B]_{ab} = E_{ab}^{(0)} + E_{ab}^{(1)} + E_{ab}^{(2)}, \quad (\text{B.1})$$

$$E_{ab}^{(0)} = (\mathcal{G}^{-1} + \theta)_{ab}^{-1}, \quad (\text{B.2})$$

$$(\mathcal{G}^{-1})^{ab} = \text{diag} \left(-G_{tt}^{-1}, G_{xx}^{-1}, \frac{G_{zz}}{G_{yy}G_{zz} + B^2}, \frac{G_{yy}}{G_{yy}G_{zz} + B^2}, (G_{\rho\rho} + L_0'^2 G_{LL})^{-1}, \right. \\ \left. G_{\eta\eta}^{-1}, G_{\xi_1\xi_1}^{-1}, G_{\xi_2\xi_2}^{-1} \right), \quad (\text{B.3})$$

$$\theta^{23} = -\theta^{32} = -\frac{B}{G_{yy}G_{zz} + B^2}, \quad \text{others zero}, \quad (\text{B.4})$$

$$E_{ab}^{(1)} = E_{Sab}^{(1)} + E_{Aab}^{(1)}, \quad (\text{B.5})$$

$$E_{Sab}^{(1)} = 2L_0' G_{LL}(L_0) \delta_{(a}^\rho \partial_{b)} \chi + \chi \partial_L G_{ab}(L_0) + L_0'^2 \chi \delta_a^\rho \delta_b^\rho \partial_L G_{LL}(L_0), \quad (\text{B.6})$$

$$E_{Aab}^{(1)} = 0, \quad (\text{B.7})$$

$$E_{ab}^{(2)} = E_{Sab}^{(2)} + E_{Aab}^{(2)}, \quad (\text{B.8})$$

$$E_{Sab}^{(2)} = G_{\Phi\Phi}(\partial_a \phi)(\partial_b \phi) + G_{LL}(\partial_a \chi)(\partial_b \chi) + 2\delta_{(a}^\rho (\partial_{b)} \chi) \chi L_0' \partial_L G_{LL}(L_0) \quad (\text{B.9})$$

$$+ \frac{1}{2} \delta_a^\rho \delta_b^\rho L_0'^2 \chi^2 \partial_L^2 G_{LL}(L_0) + \frac{1}{2} \chi^2 \partial_L^2 G_{ab}, \quad (\text{B.10})$$

$$E_{Aab}^{(2)} = 0. \quad (\text{B.11})$$

Here, we split the inverse of $E^{(0)}$ further into its symmetric (the “open string metric”) \mathcal{G}^{-1} and its antisymmetric part (the “noncommutativity parameter”) θ , as well as the linear and quadratic fluctuation parts. Note that the antisymmetric parts at linear and quadratic order vanish.

We now pull out the $E^{(0)}$ from the square root in the DBI action and use the usual determinant expansion to obtain the fluctuation part of the DBI action, dropping a factor

$$-T_7/g_s,$$

$$\mathcal{L}_{DBI}^{(2)} = \frac{1}{2}\sqrt{-\det E^{(0)}} \left[\text{Tr}(E^{(0)-1}E^{(2)}) + \frac{1}{4}(\text{Tr}(E^{(0)-1}E^{(1)}))^2 \right] \quad (\text{B.12})$$

$$+ \frac{1}{4}(\text{Tr}(E^{(0)-1}F))^2 + \frac{1}{2}\text{Tr}(E^{(0)-1}E^{(1)})\text{Tr}(E^{(0)-1}F) \quad (\text{B.13})$$

$$- \frac{1}{2}\text{Tr}(E^{(0)-1}E^{(1)})^2 - \frac{1}{2}\text{Tr}(E^{(0)-1}F)^2 - \text{Tr}(E^{(0)-1}E^{(1)}E^{(0)-1}F) \Big], \quad (\text{B.14})$$

$$\sqrt{-|E^{(0)}|} = \sqrt{\left(\prod_{M \in \{t, x, \eta, \xi_1, \xi_2\}} G_{MM} \right) (G_{yy}G_{zz} + B^2)(G_{\rho\rho} + L_0'^2 G_{LL})}. \quad (\text{B.15})$$

Because the antisymmetric parts (B.7) and (B.11) vanish and the Φ -fluctuations only show up at second order in (B.9), it is seen by checking term by term that (B.12) includes couplings between F and χ only, but not between F or χ with ϕ , and thus $A = \chi = 0$ decouples the angular fluctuations. The ϕ -part of the DBI action thus reads

$$\mathcal{L}_{DBI, \phi}^{(2)} = \frac{1}{2}\sqrt{-\det E^{(0)}} G_{\Phi\Phi}(L_0)(\mathcal{G}^{-1})^{ab} \partial_a \phi \partial_b \phi,$$

which reduces to (3.7) for the AdS-Schwarzschild background. This reasoning, as is easily checked, also holds for the gauge field background (4.1), which is needed for the electric case.

The dangerous part, which may couple gauge field and angular fluctuations, is the Wess-Zumino part of the action to second order in the fluctuations,

$$\int_{\mathcal{M}_8} \frac{1}{2} P[C_4] \wedge F \wedge F + P[\tilde{C}_4] \wedge P[B] \wedge F,$$

which could in principle introduce couplings of F to $\partial_t \phi$, $\partial_x \phi$ and $\partial_t \partial_\rho \phi$ or $\partial_x \partial_\rho \phi$, as the magnetic dual of the Ramond-Ramond four-form potential includes Φ -fluctuations, $P[\tilde{C}_4] \propto \partial_a \phi$ (see eq. (45) in [23]). With the ansatz (3.6), which does not depend on t or x , these couplings vanish. Thus $\chi = 0$, $A = 0$ and the ansatz (3.6) yields (3.7).

For the electric case, the Wess-Zumino action does lead to additional couplings for a nontrivial gauge field background F_0 . As for the Minkowski embeddings no gauge background is needed for consistency, the ansatz (4.1) used to calculate the spectrum at zero temperature is consistent. The new couplings, which spoil the above reasoning for the singular shell embeddings, are again due to the magnetic dual of C_4 , namely $\int P[\tilde{C}_4] \wedge F_0 \wedge F$. As $P[\tilde{C}_4]$ contains $\partial_a \phi d\xi^a$, this induces the following couplings (schematically): $(\partial_y \phi)(F_{zx} + F_{zt}) + (\partial_z \phi)(F_{xy} + F_{ty})$. These couplings vanish only if $\phi(\rho)$ is a function independent of all Minkowski coordinates, i.e. a zero mode in the Minkowski directions, $(\omega, k_1, k_2, k_3) = 0$. Furthermore imposing $h(\rho)$ to be normalizable singles out a unique solution. Thus for calculating the fluctuation spectrum of singular shell embeddings, in order to prove the expectation that the mesons are in a dissociated state and to clarify the role of the conically singular embeddings for the expected dissociation transition, it will be necessary to solve coupled partial differential equations for the gauge field and ϕ , most likely with numerical methods generalizing those used in [30].

References

- [1] A. Karch and E. Katz, JHEP **0206**, 043 (2002) [arXiv:hep-th/0205236].
- [2] J. Babington, J. Erdmenger, N. J. Evans, Z. Guralnik and I. Kirsch, Phys. Rev. D **69**, 066007 (2004) [arXiv:hep-th/0306018].
- [3] M. Kruczenski, D. Mateos, R. C. Myers and D. J. Winters, JHEP **0405** (2004) 041 [arXiv:hep-th/0311270].
- [4] T. Sakai and S. Sugimoto, Prog. Theor. Phys. **113** (2005) 843 [arXiv:hep-th/0412141].
- [5] N. J. Evans and J. P. Shock, Phys. Rev. D **70** (2004) 046002 [arXiv:hep-th/0403279].
- [6] I. Kirsch, Fortsch. Phys. **52** (2004) 727 [arXiv:hep-th/0406274].
- [7] K. Ghoroku, T. Sakaguchi, N. Uekusa and M. Yahiro, Phys. Rev. D **71**, 106002 (2005) [arXiv:hep-th/0502088].
- [8] D. Mateos, R. C. Myers and R. M. Thomson, Phys. Rev. Lett. **97**, 091601 (2006) [arXiv:hep-th/0605046].
- [9] T. Albash, V. G. Filev, C. V. Johnson and A. Kundu, arXiv:hep-th/0605088.
- [10] A. Karch and A. O'Bannon, Phys. Rev. D **74** (2006) 085033 [arXiv:hep-th/0605120].
- [11] C. Hoyos, K. Landsteiner and S. Montero, JHEP **0704** (2007) 031 [arXiv:hep-th/0612169].
- [12] S. Kobayashi, D. Mateos, S. Matsuura, R. C. Myers and R. M. Thomson, JHEP **0702** (2007) 016 [arXiv:hep-th/0611099].
- [13] D. Mateos, R. C. Myers and R. M. Thomson, JHEP **0705** (2007) 067 [arXiv:hep-th/0701132].
- [14] S. Nakamura, Y. Seo, S. J. Sin and K. P. Yogendran, arXiv:0708.2818 [hep-th].
- [15] S. Nakamura, Y. Seo, S. J. Sin and K. P. Yogendran, arXiv:hep-th/0611021.
- [16] K. Ghoroku, M. Ishihara and A. Nakamura, arXiv:0708.3706 [hep-th].
- [17] A. Karch and A. O'Bannon, arXiv:0709.0570 [hep-th].
- [18] A. Parnachev, arXiv:0708.3170 [hep-th].
- [19] R. Apreda, J. Erdmenger, D. Lüst and C. Sieg, JHEP **0701** (2007) 079 [arXiv:hep-th/0610276].
- [20] C. Sieg, JHEP **0708**, 031 (2007) [arXiv:0704.3544 [hep-th]].
- [21] J. Polchinski and M. J. Strassler, arXiv:hep-th/0003136.
- [22] R. C. Myers, JHEP **9912** (1999) 022 [arXiv:hep-th/9910053].
- [23] V. G. Filev, C. V. Johnson, R. C. Rashkov and K. S. Viswanathan, JHEP **0710** (2007) 019 [arXiv:hep-th/0701001].
- [24] V. G. Filev, arXiv:0706.3811 [hep-th].
- [25] A. Karch and A. O'Bannon, JHEP **0709** (2007) 024 [arXiv:0705.3870 [hep-th]].
- [26] A. O'Bannon, Phys. Rev. D **76**, 086007 (2007) [arXiv:0708.1994 [hep-th]].
- [27] T. Matsuo, D. Tomino and W. Y. Wen, JHEP **0610** (2006) 055 [arXiv:hep-th/0607178].
- [28] S. A. Hartnoll and C. P. Herzog, Phys. Rev. D **76**, 106012 (2007) [arXiv:0706.3228 [hep-th]].

- [29] T. Albash, V. G. Filev, C. V. Johnson and A. Kundu, arXiv:0709.1547 [hep-th].
- [30] T. Albash, V. G. Filev, C. V. Johnson and A. Kundu, arXiv:0709.1554 [hep-th].
- [31] M. Gell-Mann, R. J. Oakes and B. Renner, Phys. Rev. **175** (1968) 2195.
- [32] P. Aschieri, Nucl. Phys. B **617**, 321 (2001) [arXiv:hep-th/0106281].
- [33] N. Seiberg and E. Witten, JHEP **9909**, 032 (1999) [arXiv:hep-th/9908142].
- [34] N. Seiberg, L. Susskind and N. Toumbas, JHEP **0006**, 021 (2000) [arXiv:hep-th/0005040].
- [35] R. Gopakumar, J. M. Maldacena, S. Minwalla and A. Strominger, JHEP **0006**, 036 (2000) [arXiv:hep-th/0005048].
- [36] J. L. F. Barbon and E. Rabinovici, Phys. Lett. B **486**, 202 (2000) [arXiv:hep-th/0005073].
- [37] E. Witten, Adv. Theor. Math. Phys. **2** (1998) 505 [arXiv:hep-th/9803131].
- [38] C. P. Burgess, Nucl. Phys. B **294** (1987) 427.
- [39] V. V. Nesterenko, Int. J. Mod. Phys. A **4** (1989) 2627.
- [40] C. Bachas and M. Porrati, Phys. Lett. B **296** (1992) 77 [arXiv:hep-th/9209032].
- [41] C. Bachas, Phys. Lett. B **374** (1996) 37 [arXiv:hep-th/9511043].
- [42] D. Teaney, private communication.
- [43] G. B. Arfken and H. J. Weber, “Mathematical Methods For Physicists,” Academic Press, 5th edition.
- [44] M. Kruczenski, D. Mateos, R. C. Myers and D. J. Winters, JHEP **0307** (2003) 049 [arXiv:hep-th/0304032].
- [45] R. Harnik, D. T. Larson and H. Murayama, JHEP **0403** (2004) 049 [arXiv:hep-ph/0309224].
- [46] R. Apreda, J. Erdmenger, N. Evans and Z. Guralnik, Phys. Rev. D **71** (2005) 126002 [arXiv:hep-th/0504151].
- [47] D. Mateos, S. Matsuura, R. C. Myers and R. M. Thomson, arXiv:0709.1225 [hep-th].
- [48] N. Wyllard, Nucl. Phys. B **598**, 247 (2001) [arXiv:hep-th/0008125].

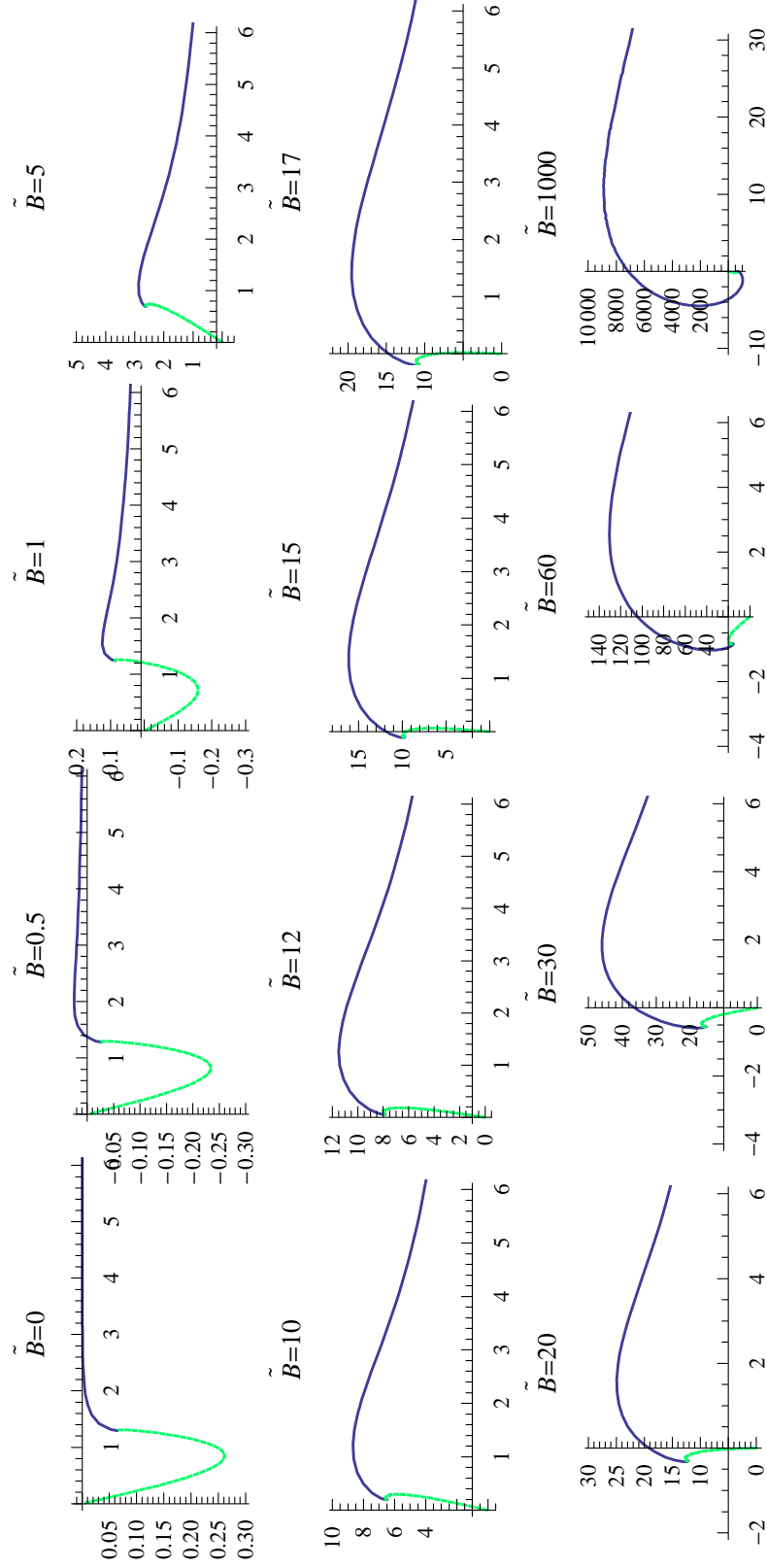


Figure 17: Condensate $\frac{8\langle\bar{q}q\rangle}{\sqrt{\lambda}N_c T^3}$ against quark mass $\frac{2m_q}{\sqrt{\lambda}T}$ for the magnetic ansatz for increasing \tilde{B} from 0 to 1000. There is a critical value of $\tilde{B} \approx 16$, above which there is no melted phase. Note the return of the spiral behaviour seen in figure 2 for large \tilde{B} .

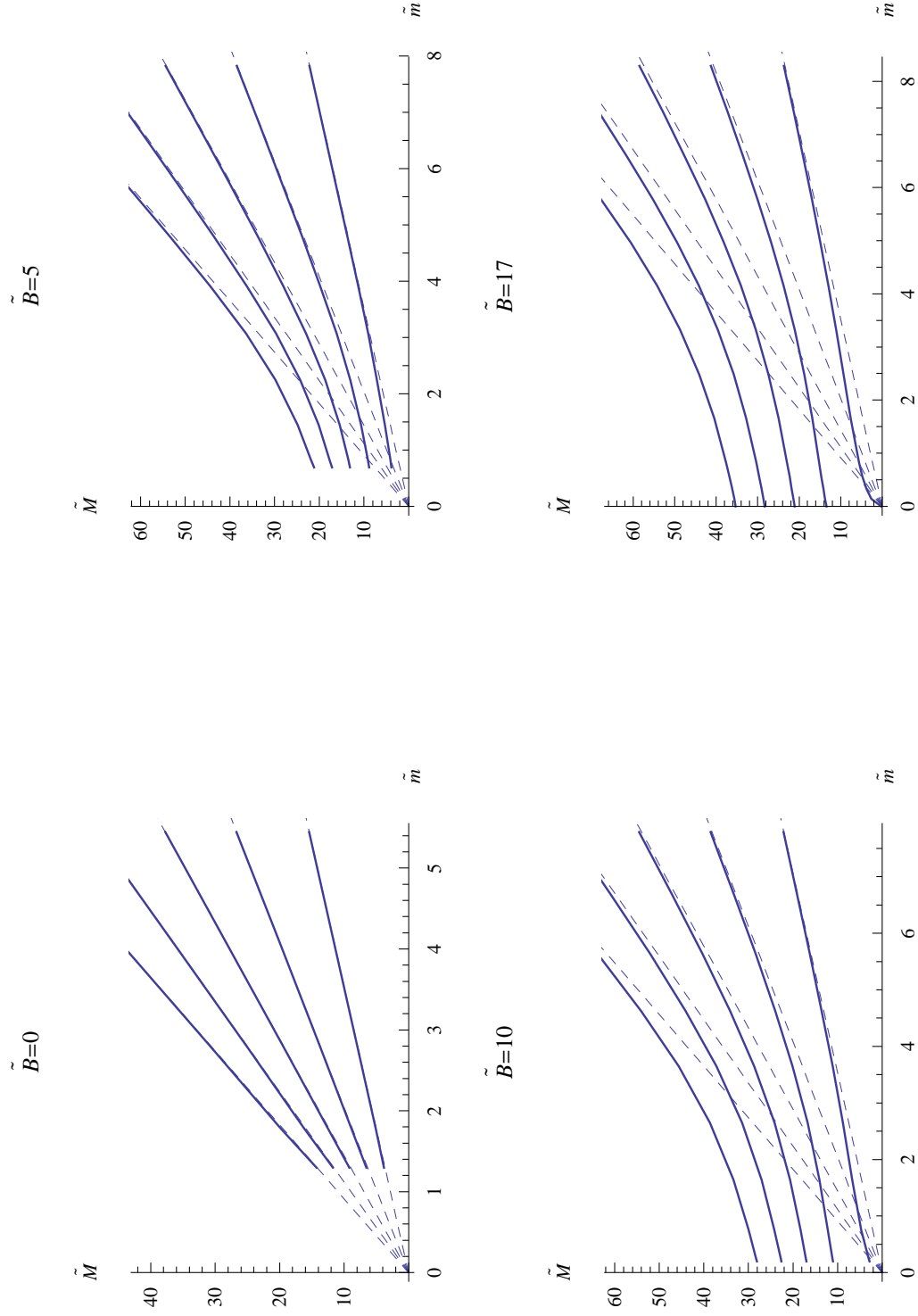


Figure 18: Meson masses for the AdS-Schwarzschild black hole background for different magnetic field strengths. The dashed lines are the pure AdS result $\tilde{M} = 2\tilde{m}\sqrt{(n+1)(n+2)}$, cf. [44]. Above the critical field strength $\tilde{B}_{crit} \approx 16$ the lowest meson state becomes massless at zero quark mass and thus is identified with the Goldstone boson of chiral symmetry breaking.